Title page

University of Zurich[UZH]

Spring Semester 2013 Prof. Dr. A. Schilling

Master Thesis

Optical Characterization of Quantum Dots

Michael Locher

Advisor: Dr. Stefan Fält
Co-Advisor: Dr. Martin Kroner

Contents

List of Figures

List of Tables

Chapter 1

Acknowledgement

First, I would like to thank **Prof. Dr. Wegscheider** and **Prof. Dr. Imamoglu** for giving me the opportunity to join their groups during my master thesis. It was an enriching expierence both at scientific as well as personal level. Thank you for your patience, optimism in all moments and the possibility to run for your team in the SOLA-Stafette. I also want to thank **Prof. Dr. Schilling** for his support and answering thousands of questions.

Thanks **Dr. Fält**, **Dr. Stumpf** and **Dr. Kroner** for introducing me to the experimental work in G20 and G13 and your great explanations. Thanks to you I learned a lot, not only about phyiscs.
Thanks **Dr. Feil** for the discussions we had about physics in general, it was exciting and instructive. **Dr. Srivastrava**, thank you much for your help, the nice sightseeing and your effort in teaching me the suisse geography.
Meinrad, thanks for your help with theoretical questions and for many funny moments we had inside and outside the ETHZ. **Yves**, I really appreciate your help you offered me although you had much trouble at the same time yourself; thanks much. **Dimitri** thanks to your special humour the work was sometimes really pleasant. Thanks **Priska**, for answering so many questions and printing me some informative papers. Thank you **Wolf** and **Adrian**, it was really cool with you guys and for your great support also in rough situations!
To all members of the quantum photonics group and advanced semiconductor quantum materials.

Outside ETHZ, I want to thank my great colleagues, **Jessica**, **Pascal**, **Philipp**, **Markus** and my **family** who not only were a great support but also for the very special moments we had, you are simply great.

Chapter 2

Introduction

Semiconductor materials find applications as solar cells, transistors, lasers and many more due to their optical and electrical properties. Although they are already a fixed part in everyday use they are still of great interest for scientists and engineers. In particular, the semiconductor nanostructures that confine charge carriers in all spatial dimensions, termed quantum dots (QD), are intensively studied since the 80s. As a result of the quantum confinement, the energy states of the trapped particles are discrete, which makes them interesting for technological applications as well as research objects in fundamental science.
QDs can be made using a variety of methods (top down: lithography, bottom-up: colloidal synthesis, epitaxy). The applied fabrication method depends, among other, on the composition of the semiconductor. For example II-VI structures are most often created by colloidal synthesis, whereas the majority of III-V heterostructures compounds like InAs/GaAs QD are grown using the molecular beam epitaxy technique. The potential felt by the electron and holes trapped inside a QD forming excitons, can be tuned during the growth by the different growth parameters (temperature, composition, deposition rate, ...). But also later, by embedding QD into a diodestructure, the discrete energy states of the QD can be tuned in a controlled manner by the application of a gate voltage to create different excitonic states [1, 2, 3].

To know about the functionality of newly grown QD samples and if they match requirements like density or emission wavelength, they are characterized by photoluminescence (PL) spectroscopy . Photoluminescence spectroscopy is a rather simple and yet powerful noninvasive method to test the optical properties. The sample is illuminated with laser light to

excite the electrons above the energy states of the QD. The photo generated electrons and holes relax into the QD and form excitons which decay under the emission of photons. The photons are collected and their energy spectrum is measured. In order to perfom PL measurements of single QDs, the samples are mounted in a fiber-based confocal microscope for cryogenic spectroscopy [4].
The focus of this work was on the implementation of the above-mentioned system for fast characterization of QD samples.

This thesis is structured as follows:
Chapter 3 gives a qualitative description of QDs, in particular self-assembled QDs and their optical properties.
Chapter 4 explains the methods of PL spectroscopy and resonant spectroscopy. The theoretical framework of the interaction between a two-level quantum emitter and an electromagnetic field is presented.
In Chapter 5, the experimental tools for probing a single QD are presented in more detail. Chapter 6 gives a more detailed description of the samples used, a field-effect device and micropillars, along with the ability to tune the emission from the QD by means of an electric field and temperature control. Chapter 7 discusses a charging diagram of a single QD measured in PL and the power dependent resonant laser spectroscopy on the X^- state for the field-effect heterostructure and shows the resonant tuning of an exciton state into the fundamental cavity mode for a micropillar.

Chapter 3

Overview Quantum Dots

This chapter introduces QDs. Their physics and their use in science and technology are discussed in section 3.1. In the following section, 3.2, a special type of QDs is presented: self-assembled QDs, which are used in this thesis. The next two sections 3.3.1 and 3.3.2 are dedicated to the optical properties of self-assembled QDs, which are determined by the number of electrons and holes trapped in the QD, forming exciton complexes. It is shown, that they can be identified by means of their spectra and power dependency.

3.1 Quantum Dots in science and technology

QD are semiconductor nanostructures that are in all spatial dimensions smaller than the de-Broglie wavelength[1] [3],

$$\lambda_{\text{de Broglie}} = \frac{h}{p} = \frac{h}{\sqrt{2 m_{\text{eff}} k_{\text{B}} T}}. \tag{3.1}$$

In equation 3.1, h and k_{B} are Plancks' and Boltzmanns' constant, p the momentum and m_{eff} the effective mass of the carrier.

The confinement of particles on the nanoscale leads to quantization effects, resulting in discrete energy states known from the case of an electron trapped to the nucleus of an atom. Further the single energy states (shells) of QDs can, similar to atoms, be occupied by electrons under consideration of the Pauli exclusion principle and Hunds rule [5]. This allows to recreate many phenomena observed in atoms [6]. Although QD and atoms show

[1] The de-Broglie wavelength sets the boundary at which the quantum mechanical nature of a particle emerges.

commonalities, they also differ at some points. Among them is the fact that QD are crystalline structures consisting of 10^4 to 10^5 atoms giving rise to phonon scattering and lattice defects influencing the energy states and optical transitions [1]. Also the quantization effects in QD are in the range from tens of meV up to several 100 meV compared to 1 eV up to 10 keV in isolated atoms [7]. Consequently QDs must be cooled down ($\ll 50$ K[2]) to suppress the electron phonon interaction and be able to observe the quantum size effects.

But QD are not only limited to the simulation of real atoms, but exhibit new physics due to their mesoscopic nature: The QD potential felt by the electrons can be tailored during the growth (see 3.2) and tuned afterwards by embedding QD in a field-effect structure, enabling the charging of the QD with electron holes and tuning the emission wavelength (see 6.1). A single electron or hole trapped in the QD can be used to study single electron interactions with the environment such as the study of quantum dot nuclear spin systems and their coupling to confined electron spins [9] or many-body correlations [10]. Also very promising are QD in the study of Cavity-QED phenomena [11]. Besides the attractivity in the fundamental science have QD furthermore a great potential for technological applications. This is because, in addition to their quantum nature, they are made of semiconductor materials like the conventional computer chips in use.
For example their great tunabiltiy of the emission wavelength from the ultraviolet to the infrared region can be used for new types of LED (white light with high color-rendering index [12]) or as efficient absorber in solar panels. Additionally their short radiative lifetimes (1 ns) make them interesting as practical candidates[3] for single photon sources [13].

3.2 Self-assembled Quantum Dots

The investigated QD in this thesis are InAs QD embedded in GaAs matrix grown with the use of an advanced crystal growth technique, the molecluar beam epitaxy (MBE). The driving force behind the growth of QD by MBE is the lattice mismatch between GaAs and InAs (7 %). The deposition of

[2] true for self-assembled InAs/GaAs QD, Gallium Nitride QD has shown photon anti-bunching statistics up to 200 K, demonstrating high-temperature quantum effects [8]

[3] practical means: single photon emission at room temperature, bit rate > 10 Mbps, emission wavelength around 1.55 μm

a thin InAs layer on top of GaAs forms a strained layer, the wetting layer. This strain increases further by increasing the wetting layer thickness. At a critical thickness of the InAs (1.7 monolayer) the accumulated strain is relieved by the epitaxial islanding transition [14]. This transition leads to the formation of three dimensional systems, the QD (see figure: 3.2). The obtained QD have typical dimensions of approximately 15-30 nm in diameter and 4-5 nm in height. Although the MBE allows for a very good control over the growth procedure, the QD created by the strained layer epitaxy are not completely uniform but varies slightly in size, geometry and in material composition. This affects the potential felt by the charge carriers and thereby their energy states [15, 16]:

size: the smaller the potential well the greater the energy differences between the states in the QD

composition: the material composition determines the band edges of the semiconductor and with it the depth of the confinement potential

shape: affects the overlap of the electron and hole states and with it the interaction energy and oscillator strength

The exact details between the relation of the structural parameters and the optical properties are complex and still a current field of study [17].
The nonuniformity of the QDs leads to inhomogenously broadened spectra if several QDs are probed simultaneously:
For a typical QD density of around 10^{10} to 10^{11} cm^{-2} and a conventional micro-photoluminescence (μPL) setup with a spatial resolution of 1 μm up to 1000 slightly different QDs are present under the laser spot. Their spectra superimpose to give broad ensemble peaks. The inhomogenously broadening limits the resolution of the experiments on 50 to 100 meV [18] and thus do not allow to study single QDs and their properties [19]. In figure 3.1 the PL spectrum of a QD ensemble is shown.

The study of single QDs can be achieved by a strong reduction of the density (gradient growth technique, see 6.1) and the use of a confocal microscope, discussed in 5.3.

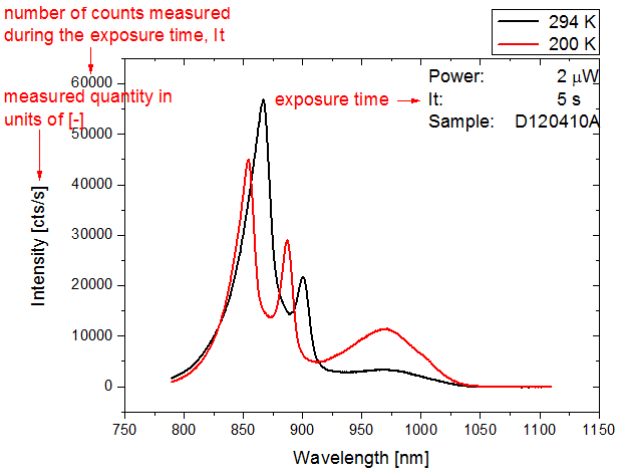

Figure 3.1: At the center wavelength of the QD the inohomogenously broadened peak can be seen (for comparison a single QD linewidth is around 0.7 pm). Further it can be seen the competition between the different states: at high temperatures the thermal energy is too high such that the electrons cannot be efficiently trapped in the QD, the emission for the continuum states in the Wetting Layer (WL) and the bulk Gallium Arsenide (GaAs) is high. At lower temperatures the thermal energy of the electrons decrease leading to higher populated states in the QD. Furthermore, explanations are given (written in red) for the correct reading of the shown data.

3.3 Identification of QD excitons

3.3.1 Energies of the complex excitons

The ground state of a semiconductor corresponds to a completely occupied valence band and an empty conduction band. A simple excitation of this two level system is to lift an electron into the conduction band, which leaves a hole state in the valence band and is called an electron-hole excitation, described by

$$H_{eh} = H_e + H_h. \tag{3.2}$$

Where $H_{e/h}$ are the single-particle Hamiltonians of electron and hole. Taking into account the Coulomb interaction, C_{eh}, between electron and holes there is another class of excitations called excitons:

$$H_X = H_e + H_h + C_{eh}. \tag{3.3}$$

In bulk semiconductors the Coulomb interaction between the charged carriers leads to bound states just below the band gap of the semiconductor.

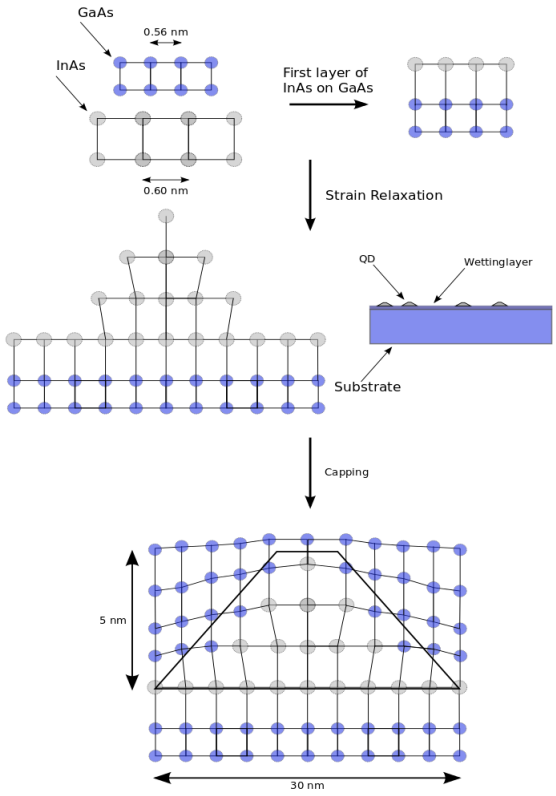

Figure 3.2: Shown is the traditional growth mechanism of QDs: The phase transition from an inital unstrained InAs layer to a 3 dimensional island, QD, due to the lattice mismatch between the semicondcutor materials. We will discuss in section 6.1.1 the so called partially covered island growth mode an additional step in which the height of the QDs is reduced to 2 - 3 nm to blue shift their emission wavelength.

The binding energy of the exciton is given in the effective mass approximation by

$$E_X(n,\vec{K}) = E_g - Ry\frac{\mu}{\epsilon^2}\frac{1}{n^2} + \frac{\hbar\vec{K}^2}{2M}. \tag{3.4}$$

With n = principal quantum number, $\vec{K} = \vec{k_e} + \vec{k_h}$ the exciton wave vector, E_g the band gap, R_y the Rydberg constant: 13.6 eV, μ the reduced mass: $\frac{1}{\mu} = \frac{1}{m^e_{\text{eff}}} + \frac{1}{m^h_{\text{eff}}}$, ϵ the dielectric constant and M the mass of the exciton: $m^e_{\text{eff}} + m^h_{\text{eff}}$.

The effective masses of the electron and hole are defined by the curvature

of the energybands

$$m^* \quad := \quad m_{\text{eff}}^{e,h} = \quad \hbar^2 \cdot \left(\frac{\delta^2 E_i}{\delta k^2} \right)^{-1} . \tag{3.5}$$

This description is only true for the Warnier excitons where their Bohr radius extends over several lattice constants and the Coulombic interaction is strongly screened such that their energy-levels lie within the band gap of the semiconductor [16, 20]. The most appropriate value for the electron and hole effective-mass in InAs/GaAs quantum dots is believed to be the electron effective-mass in bulk GaAs and the vertical heavy-hole effective-mass in bulk InAs, respectively [21].

In QDs no free electron-hole pair exists because the Coulomb interaction is enhanced with respect to the bulk case due to the close proximity of the wavefunctions. Because no free carrier exist in QDs a spectroscopical investigation of the the excitonic binding energies is not possible, but theory predicts binding energies in the range of 20 - 30 meV as compared to 4.2 meV in the bulk [22, 23]. The strong confinement of particles inside of QD facilitates the observation of charged excitons, for example trions X^+, X^-, which are only very weakly in bulk semiconductors [24, 25].

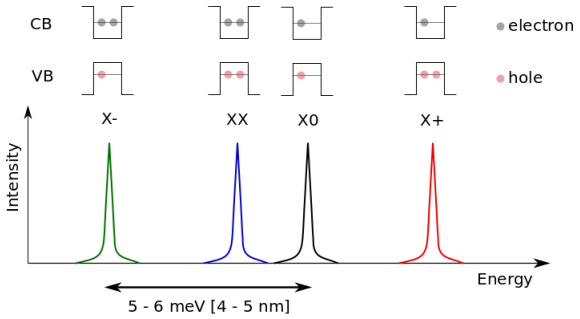

Figure 3.3: The relative position of excitonic states by taking only into account the Coulomb interaction between the electron and hole wavefunction. The biexciton and positive trion can be located on either side of the neutral exciton. In contrast, is the negatively charged exciton always 5 - 6 meV shifted to the low energy side of the neutral exciton for InAs/GaAs QDs (private communication Dr. Martin Kroner).

The energies of the exciton configurations: X^0, X^+, X^-, XX^0 can be described in terms of the quantized energy states of the QD and the Coulomb interaction among the electrons and holes trapped in the QD [26]

$$H = \sum_i E_i^e c_i^+ c_i + \sum_i E_i^h d_i^+ d_i - \sum_{ijkl} \langle ij|C_{eh}|kl\rangle \, c_i^+ d_i^+ d_k c_l$$
$$+ 1/2 \sum_{ijkl} \langle ij|C_{ee}|kl\rangle \, c_i^+ c_j^+ c_k c_l + 1/2 \sum_{ijkl} \langle ij|C_{hh}|kl\rangle \, d_i^+ d_j^+ d_k d_l, \quad (3.6)$$

where c_i^+, d_i^+ (c_i, d_i) are the creation (annhilation) operators for electons and holes. $E_i^{e/h}$ are the electron single particle energies which can be expressed, in the "Dalgarno model" [27], with the ionization energy E_c, the effective energy-gap E_g and C_{ij} (see figure 6.4), ij = e,h the interparticle Coulomb interactions:

$$C_{ij} = \frac{e^2}{4\pi\epsilon_0\epsilon} \int\int \frac{\|\Psi_i(\vec{r})\|^2 \|\Psi_j(\vec{r})\|^2}{\|\vec{r}_1 - \vec{r}_2\|} d\vec{r}_1 d\vec{r}_2. \quad (3.7)$$

The energies of the various excitonic complexes reads then as

$$E(X^0) = E_g - C_{eh}, \quad (3.8)$$
$$E(X^-) = E_g + E_{V_g} - E_c - 2C_{eh} + C_{ee}, \quad (3.9)$$
$$E(X^+) = 2E_g - E(V_g) + E_c - 2C_{eh} + C_{hh}, \quad (3.10)$$
$$E(XX^0) = 2E_g - 4C_{eh} + C_{hh} + C_{ee}. \quad (3.11)$$

The difference in the PL energies (energy difference between initial and final state) among the states

$$E_{PL}(X^-) - E_{PL}(X^0) = -C_{eh} + C_{ee}, \quad (3.12)$$
$$E_{PL}(X^+) - E_{PL}(X^0) = -C_{eh} + C_{hh}, \quad (3.13)$$
$$E_{PL}(XX^0) - E_{PL}(X^0) = -2C_{eh} + C_{hh} + C_{ee}. \quad (3.14)$$

The energy differences are completely described by the attractive C_{eh} and the repulsive C_{hh}, C_{ee} Coulomb terms. The energetical position in the spectrum of the trions compared to the neutral exciton can thus be obtained by considering the relative strengths of the Coulomb interaction terms:

$$C_{ee} < |C_{eh}| < C_{hh}. \quad (3.15)$$

This order is in general true for InAs/GaAs QD [22]. The result in the relative position to each other is shown in figure 3.3. This serves as basis for

identifying the excitonic states during the PL measurements, in particular the fixed energy difference between X^0 and X^- of around 6 meV (private communication with Dr. Martin Kroner).
The results presented in section 7.1 show a slight deviation for the positive trion state, which is lower in energy than the neutral exciton. It is well-known that the X^+ can be red or blue shifted with respect to the X^0 and is an indication that the charging energies of holes do not follow a simple general rule that can be applied to all QDs [15, 28]. In the following section the power dependencies of the biexciton and excitonic state is compared.

3.3.2 Power Dependencies of the Excitons

Rate equations allow to study the dynamics of energy level populations such as in laser gain media, atoms or quantum dots [29]. A simple three level rate equation is able to model the emission intensity of the exciton and biexciton recombination versus the excitation power, which gives us another way to distinguish between neutral exciton and biexciton. With higher order level rate equations it is also possible to study the relative confinement regime of different QD (stronger/weaker confined systems) and information about higher lying energy states (number of occupied levels).
The three levels consist of the occupation probabilities of ground state p_0, the excitonic state p_X and biexitonic state p_{XX} and fulfill

$$p_0 + p_X + p_{XX} = 1. \tag{3.16}$$

The dynamics are given by:

$$\frac{dp_0}{dt} = -gp_0 + \frac{p_X}{\tau_X}, \tag{3.17}$$

$$\frac{dp_X}{dt} = gp_0 + \frac{p_{XX}}{\tau_{XX}} - \frac{p_X}{\tau_X} - gp_x, \tag{3.18}$$

$$\frac{dp_X}{dt} = gp_x - \frac{p_{XX}}{\tau_{XX}}. \tag{3.19}$$

The transitions which increase the number of the excitons are driven by the generation rate g; g is proportional to the excitation power, and the recombination of the biexciton ($\frac{p_{XX}}{\tau_{XX}}$). The exitonic state can be depopulated by the biexciton creation (gp_x) and the exciton recombination ($\frac{p_X}{\tau_X}$). The biexitonic popluation is only influenced by the recombination ($\frac{p_{XX}}{\tau_{XX}}$) and the generation rate (gp_x), neglecting direct creation/recombination from/to

the ground state. The emission intensities under stationary conditions ($dp_0/dt = dp_X/dt = dp_{XX}/dt = 0$) for the excitons and biexcitons are

$$I_X \propto \frac{p_X}{\tau_X} = \frac{g}{\gamma + g\tau_X + g^2\tau_x\tau_{XX}}, \tag{3.20}$$

$$I_{XX} \propto \frac{p_{XX}}{\tau_{XX}} = \frac{g^2\tau_X}{\gamma^2 + g\gamma\tau_X + g^2\tau_x\tau_{XX}}. \tag{3.21}$$

We see that the biexciton intensity increases quadratically and the excitons linearly with respect to the excitation power. Thus a power dependent measurement allows us to distinguish between biexciton and exciton. The power dependency of the emission intensity of the trions, neutral exciton and the biexciton has been measured and their characeristic linear and quadratic increase is observed.
Another identification tool for the different excitonic states in QDs is a polarization dependent measurement of the emitted photons, where some states are degenerate in energy with respect to the polarizer and other states show a splitting in energy [16]. This technique is just mentioned for completeness and is not further considered in this work.

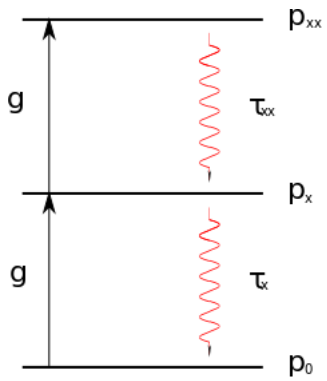

Figure 3.4: Three level scheme including exciton and biexciton state with the possible relaxation channels into the cavity mode $\Gamma(\Delta)$ and into leakage modes γ.

Chapter 4

Resonant and Non-resonant Excitation

This chapter compares the non-resonant and resonant excitation from a theoretical point of view. First the problem associated with photoluminescence applications, the poor collection efficiency, is treated and the technique of photoluminescence spectroscopy is explained. Afterwards the resonant excitation on a two-level system is discussed. By pumping a two level system resonantly, well-known phenomena such as power-broadening and power-saturation can be observed, the obtained model-functions describing these phenomena are then fitted to the measured data.

4.1 Photoluminescence

A key limitation of QDs embedded in a semiconductor medium ($n_{\mathrm{GaAs}} = 3.46$) is the low collection efficiency, as most of the emitted photons are reflected at the GaAs/air boundary[1].

A gross value for the collection efficiency of the used setup can be given by modelling the QD as a dipole emitter (see appendix B for more details, based on reference [30]). The overall probability that an emitted photon can be detected is the product of the different transmission and reflectivity grades of the optical components and the quantum efficiency of the detector[2]:

[1] Only the photons within a cone with opening angle defined by the critical angle of total reflection $\theta_c = \sin {n_{\mathrm{air}}/n_{\mathrm{GaAs}}}^{-1} = 16.8^\circ$ can be transmitted.

[2] It must be considered that all optical elements are wavelength sensitive. To simplify the calculations a monochromatic emitter with 980 nm is assumed. For polychromatic

$$\begin{aligned}\eta &= [C_{geom}] \cdot [T_{cryo}] \cdot [T_{obj}] \cdot [R_{optics}] \cdot [\eta_{spec}] \cdot [C_{SMF}] \\ &= [0.008] \cdot [0.92] \cdot [0.55] \cdot [0.5 \cdot 0.92 \cdot 0.98^2] \cdot [0.6 \cdot 0.7 \cdot 0.1] \cdot [0.4] \\ &= 3 \cdot 10^{-5}.\end{aligned}$$

C_{geom} is calculated in appendix B, η_{spec} is the average grating efficiency for s- and p-polarization, the coupling efficiency of CM5 in the spectrometer and the quantum efficiency of the detector, T_{cryo} the transmission grade of the cryo window, T_{obj} the measured transmission of the nikon objective, R_{optic} is given by the reflectivity of the bragg-mirrors, PBS and BS and C_{SMF} is the average coupling efficiency into the single mode fiber.

The collection efficiency is rather low. Assuming a spontaneous emission rate for the fundamental transition of a saturated QD of $\gamma_{spont} = 10^{-9}$ s, there should be only $3 \cdot 10^4$ detectable events. This value decreases further by taking into account the semitransparent topgate ($6 - 8$ nm) by about 30% (private communication with Dr. Martin Kroner), thus giving emission rates of approximately 10^4 photons/s.

Besides the difficulty of a weak signal, photoluminescence spectroscopy is a useful and widespread optical method for the study (energy eigenvalues of the system) and characterization (optical emission efficiency, composition of the material, impurity content, layer thickness) of different semiconductors. The basic principle in the photoluminescence spectroscopy is the analysis of the emission spectra of the optically excited (optical pumping) materials. During the optical pumping electron-hole-pairs with initially well defined phase relationship with the electromagnetic field are generated in the conduction respectively valence band. However this coherent state is quickly destroyed (timescale $<$ 100 fs) due to different scattering processes (carrier-carrier, carrier-phonon) [31, 32].

A small part of the excited electrons and holes in the conduction and valence band will directly recombine in the GaAs layer by the emission of a photon, which can be detected. The emitted photon corresponds to the difference in energy between the initial and final state. The majority will thermalise and diffuse within the accessible states: free surface, recombination centre (defect states) or the wetting layer. In the wetting layer the carriers can also recombine or lose further part of their energy through emission of

light the collection efficiency is an integral over the whole bandwidth.

optical phonons or Auger scattering, and are subsequently captured in the discrete energy states of the QD. The carriers inside the QD will further relax from the excited energy states down to the ground state on a ps timescale. The QD exciton lifetime is 1 ns and will afterwards spontaneously decay under the emission of a photon.
Thus the luminescence spectrum contains all the possible transitions in the structure and makes it difficult/impossible to study a single transition. Usually, the spectrum is analysed with a spectrometer which limits the obtainable resolution above 50 μeV.

In contrast, resonant excitation of a QD enables coherent control of the optical states under investigation. The resolution is only limited by the laser bandwidth. To get a better understandig of resonance fluorescence, the general physics of a two level system are explained below.

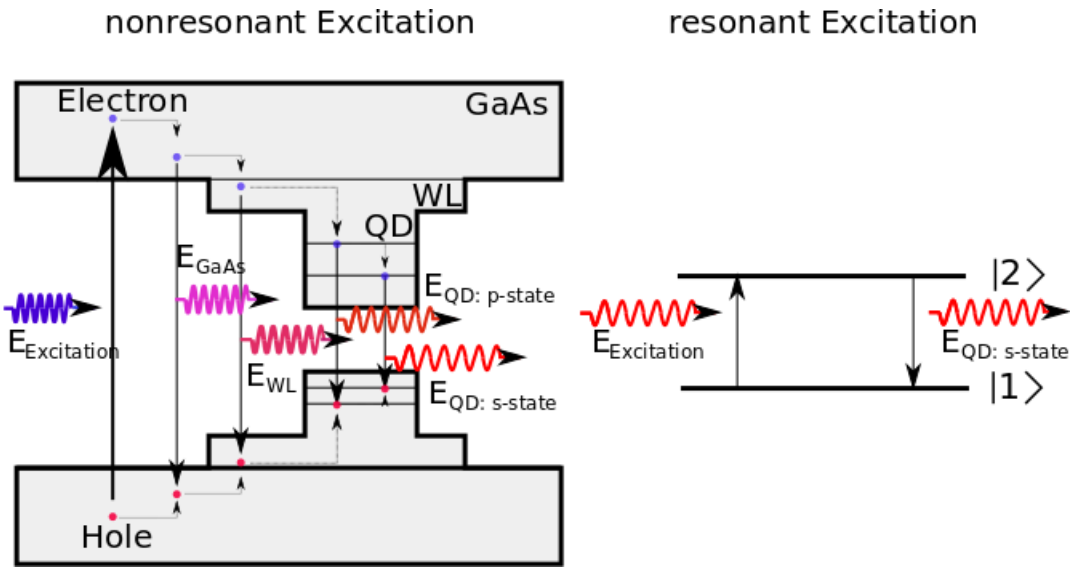

Figure 4.1: The left image shows the different relaxation chanels under emission of a photon of an electron excited into the GaAs structure, and the right the resonant pumping.

The description of two level systems is the easiest, non-trivial quantum-mechanical approach to explain the interaction between light and matter and is of fundamental importance. The strength of this model is not only the power to describe observable dynamics such as Rabi oscillations, vacuum Rabi splitting, spontaneous emission processes etc., but its universal applicability not only on single spins, but also on transitions in atoms and even in QD. The following explanations are based on the work of Tannoudji [33], Scully

[34] and mainly on Loudon's work [35].
It does not matter if the system is a real two level systems or if there are multiple states as long as the interaction between the electromagnetic field is restricted to two particular states. This is the case when the states are resonantly driven and the spectral linewidth of the applied field is smaller than the optical transitions between neighboring states. For our tunable laser we have a laser linewidth of 100 kHz (0.5 neV), which is much smaller than the expected level spacing of 0.2 eV in our QD [28]. Thus we have an effective two level system ($|\psi\rangle = c_1 |1\rangle + c_2 |2\rangle$) with transition frequency $\omega_0 = \omega_2 - \omega_1$. The Hamiltonian of the system is written as

$$H = H_A + H_I, \tag{4.1}$$

where H_A and H_I represent the quantized QD electron system and the coupling of the QD with a radiation field in dipole approximation[3]

$$\begin{aligned} H_A &= \hbar\omega_1 |1\rangle \langle 1| + \hbar\omega_2 |2\rangle \langle 2|, & (4.2)\\ H_I &= -(\varrho_{12} |1\rangle \langle 2| + \varrho_{21} |2\rangle \langle 1|) E(t). & (4.3)\\ & & (4.4) \end{aligned}$$

Where: $\varrho_{12} = \varrho_{21}^* = e \langle 1|x|2\rangle$ is the matrix element of the electric dipole moment for a lineraly polarized electric field along the x direction,
$E(t) = E_0 \cos\omega_L t$ defining the Rabi frequency $\hbar\Omega = \varrho_{12} E_0$ with E_0 the amplitude of the electric field and ω_L its frequency.
The next step in the derivation of the Hamiltonian is to apply a unitary transformation: UHU^* with $U = \exp(-i/\hbar H_A t)$ to get the Hamiltonian in the interaction picture. With the application of the rotating wave approximation and in a frame rotating at laser frequency ($\omega_L = \omega_0 + \delta$), the Hamiltonian of the system now reads [36]

$$Hs = \frac{\hbar\delta}{2} (|1\rangle \langle 1| - |2\rangle \langle 2|) + \frac{\hbar\Omega}{2} (|1\rangle \langle 2| + |2\rangle \langle 1|). \tag{4.5}$$

To include the decay of the atomic levels due to spontaneous emission we use the density matrix,

[3]The dipole approximation considers the fact that a normal two level system is usually orders of magnitude smaller than the wavelength of the laser (diameter of QD: 0.02 μm, central wavelength: 1 μm), respectively, thus the spatial variation of the applied field can be neglected at the position of the QD.

$$\hat{\rho} = \sum_{1,2} c_k \left|\psi_k\right\rangle \left\langle\psi_k\right| \tag{4.6}$$

$$= c_1^2 \left|1\right\rangle \left\langle 1\right| + c_2^2 \left|2\right\rangle \left\langle 2\right| + c_1 c_2^* \left|1\right\rangle \left\langle 2\right| + c_2 c_1^* \left|2\right\rangle \left\langle 1\right|, \tag{4.7}$$

to describe the dynamics of the quantum emitter

$$i\hbar \frac{d}{dt}\rho_{ij} = -\frac{i}{\hbar}\sum_k \left(Hs_{ik}\rho_{kj} - \rho_{ik}Hs_{kj}\right) - \frac{1}{2}\sum_k \left(\Gamma_{ik}\rho_{kj} + \rho_{ik}\Gamma_{kj}\right). \tag{4.8}$$

The first term describes a two level system that undergoes Rabi oscillations between the lower $|1\rangle$ and upper state $|2\rangle$. The coupling term to the environment $(\Gamma, \hat{\varrho})$ perturbs the phase relationship between the driving radiation field and the quantum emitter. After some time, the phase relation is completely randomized and the Rabi oscillations declines (dephasing). The process of dephasing leads in a natural way to a broadening of the otherwise monochromatic emission.

The phenomenon of dephasing can be modeled with a damped harmonic oscillator and will lead to the spectral profile observable from the optical radiation of an excited two level system [37].
The initial excited harmonic oscillator will decay to its equilibrium state because of the restoring force (damping). The damping leads therefore to a decrease of the amplitude and with it to a continous modulation of the oscillating frequency. The change of the initial monochromatic frequency is revealed due to a Fourier transformation of the corresponding amplitude $A(t) = A_0 \exp(-\gamma t)\cos\omega_0 t$, which results in

$$I(\omega) = I_0 \frac{\gamma^2}{(\omega - \omega_0)^2 + \gamma^2}. \tag{4.9}$$

The power spectrum 4.9 is described by a Lorentzian profile. This is in general true for an exponentially damped system. The linewidth Γ_0 is defined by the full width half maximum (FWHM): $2{\cdot}\gamma$ [Hz] [4] and its peak I_0.

The natural linewidth is a lower bound for the actual linewidth of a system. For a QD the natural linewidth is stated to be 0.8 μeV (by private communication with Dr. Martin Kroner). However, this line can usually not be directly resolved because of the resolution limits of the used equipment (5.5.3) and due to homogenous broadening processes affecting the system [28].

[4] The linewidth in section 7.2 is expressed in units of energy: $\Gamma_0 = 2\hbar\gamma$.

Using 4.8 the equations of motion for the density matrix elements read

$$\frac{d}{dt}\rho_{11} = \gamma\rho_{22} + i\frac{\Omega_0}{2}(\tilde{\rho}_{21} - \tilde{\rho}_{12}), \tag{4.10}$$

$$\frac{d}{dt}\rho_{22} = -\gamma\rho_{22} + i\frac{\Omega_0}{2}(\tilde{\rho}_{a12} - \tilde{\rho}_{21}), \tag{4.11}$$

$$\frac{d}{dt}\tilde{\rho}_{12} = -\left(\frac{\gamma}{2} + i\delta\right)\tilde{\rho}_{12} + i\frac{\Omega_0}{2}(\tilde{\rho}_{22} - \tilde{\rho}_{11}), \tag{4.12}$$

$$\frac{d}{dt}\tilde{\rho}_{21} = -\left(\frac{\gamma}{2} - i\delta\right)\tilde{\rho}_{21} + i\frac{\Omega_0}{2}(\tilde{\rho}_{11} - \tilde{\rho}_{22}). \tag{4.13}$$

With: $\tilde{\rho}_{21} = \rho_{21}\exp(i\omega_L t)$, $\tilde{\rho}_{12} = \rho_{12}\exp(-i\omega_L t)$, $\gamma = \gamma_{\text{spont}} + \gamma_{\text{coll}}$ is the total decay rate taking also into account collision broadening, and the corresponding elements of the density matrix are

$$\rho_{11} = c_1(t)^2, \tag{4.14}$$

$$\rho_{22} = c_2(t)^2, \tag{4.15}$$

$$\rho_{12} = c_1(t)c_2(t)^*, \tag{4.16}$$

$$\rho_{21} = c_2(t)c_1(t)^*. \tag{4.17}$$

Where the on diagonal elements ρ_{11}/ρ_{22} are the probabilities of being in the upper and lower state, respectively, and the off diagonal elements ρ_{12}/ρ_{21} represent the coherent nature of the system.

To calculate the number of scattered photons, stationary conditions are assumed. This is justified for a continously pumped system, where the excitation power is constant in time, such that the number of generated and recombined excitons does not change. The steady state solution of the upper state is then given by

$$\rho_{22} = \frac{(\gamma/4\gamma_{\text{spont}})\,\Omega_0^2}{(\omega_0 - \omega_L)^2 + \gamma^2 + (\gamma/2\gamma_{\text{spont}})\,\Omega_0^2}, \tag{4.18}$$

and describes the well-known saturation phenomena. Its effective linewidth is given by

$$\text{FWHM} = 2\left(\gamma^2 + \gamma/2\gamma_{\text{spont}}\Omega_0^2\right)^{1/2}. \tag{4.19}$$

The FWHM of the Lorentzian function is also power dependent and describes only for a vanishing incident field ($E_0 \to 0$) the natural linewidth of the system. This effect is called power broadening and comes from the

fact that the scattering rate is limited by the the lifetime $\tau = 1/\gamma$ of the excited state, thereby setting a fundamental boundary for the scattering rate of a two level system.
The production rate of scattered photons by a single two level system and collected by the optical setup equals to:

$$\mathrm{R} = \frac{(\gamma/4\gamma_{\mathrm{spont}})\,\Omega_0^2}{(\omega_0-\omega_L)^2+\gamma^2+(\gamma/2\gamma_{\mathrm{spont}}\Omega_0^2)} \cdot [2\gamma_{\mathrm{spont}}\eta] \tag{4.20}$$

By introducing the on-resonance, $(\omega_0-\omega_L)^2 = 0$, the saturation parameter equals

$$\frac{P}{P_{\mathrm{sat}}} = \frac{\Omega_0^2}{2\gamma\gamma_{\mathrm{spont}}}. \tag{4.21}$$

A problem caused by fitting equation 4.20 to the datapoints shown in section 7.2 due to overfitting can be circumvented[5]. The obtained formula reads (by private communication with Yves Delley)

$$\mathrm{R} = \frac{b\quad\frac{P}{P_{\mathrm{sat}}}}{\left(1+\frac{P}{P_{\mathrm{sat}}}\right)} \tag{4.22}$$

and its corresponding FWHM

$$\mathrm{FWHM} = 2\cdot\sqrt{\gamma^2\left(1+\frac{P}{P_{\mathrm{sat}}}\right)}. \tag{4.23}$$

With $b = \eta\cdot\gamma_{\mathrm{spont}}$. These model-functions describing these phenomena are then fitted to the measured data in section 7.2.

[5]The term $\left(\gamma/2\gamma_{\mathrm{spont}}\Omega_0^2\right)$ caused trouble to determine γ and γ_{spont} because Ω_0 is unknown and cannot be read out of the data similar to make a linear regression with a function of the form: $y = abx + c$, where a, b and c are the parameters to be determined.

Chapter 5

Optical Setup

The fifth chapter is dedicated to the optical setup. Section 5.1 introduces the optical setup. The following section 5.2 discusses Gaussian modes, which model the laser profile accurately, and the expected spatial resolution of the optical setup is calculated. The second section explains the principle and advantages of confocal microscopy with regard to single QD spectroscopy 5.3.

The most important issue in the installation of an optical setup (apart from correct alignment of the beam path) are matching optics for optimal imaging and coupling efficiencies, discussed in the two sections 5.3.1 and 5.3.2. In the next two sections the focus lies on the practical part of the two excitation schemes: how to excite the sample non-resonantly (5.4) and resonantly (5.5), where the tunable laser (5.5.1), the cryogenics (5.5.2) and the spectrometer (5.5.3) plays a central role. The complete alignment procedure to reproduce the results obtained in this thesis is discussed in the appendix (A).

5.1 Optical Setup for Single QD Spectroscopy and Characterization

The requirements for an optical setup for μPL measurements are manifold and depend on the exact type of measurement to be performed. In general the optical setup requires a high stability over a long period of time as well as high spectral and high spatial resolution.

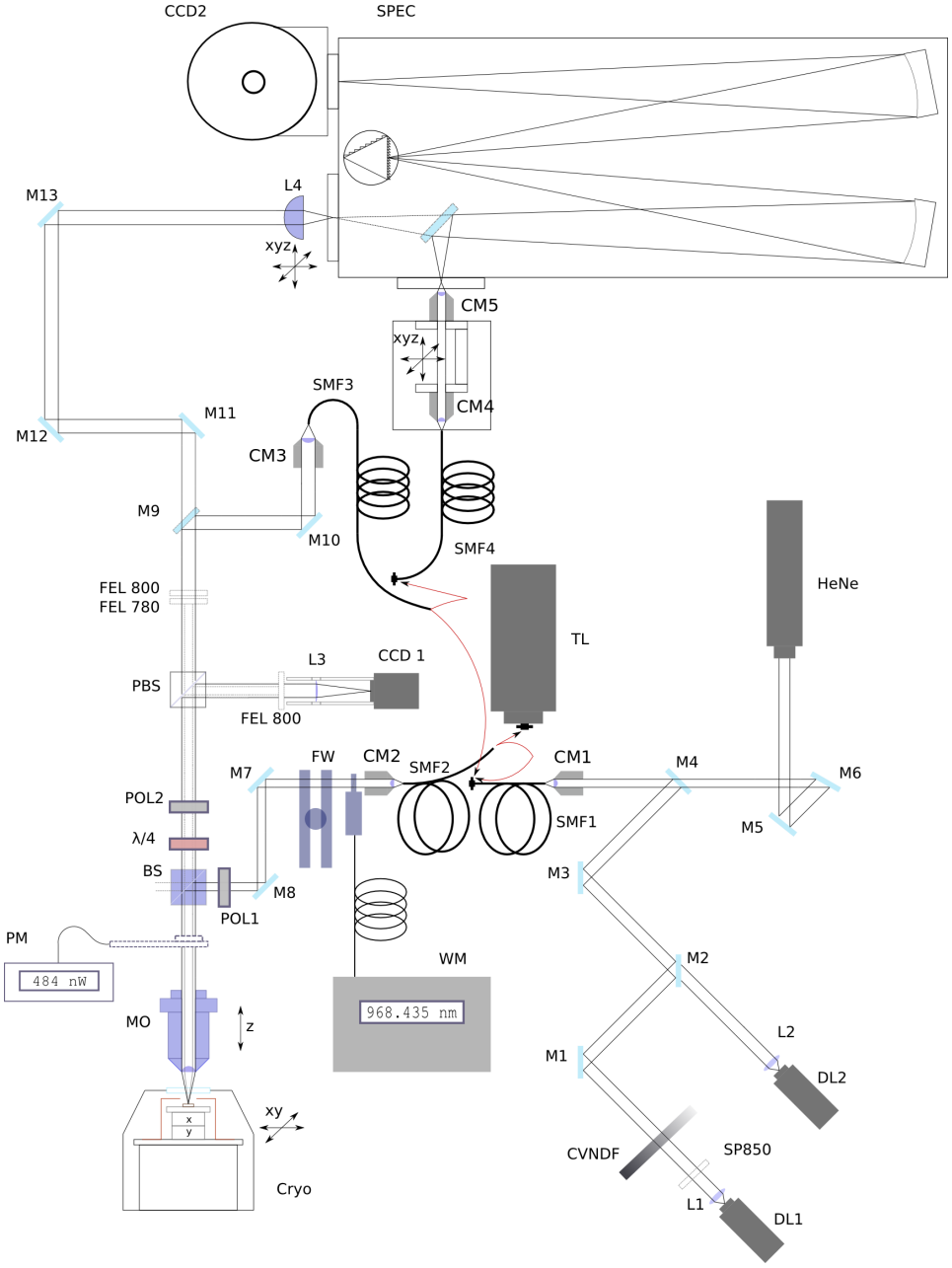

Figure 5.1: Overall experimental optical setup for sample characterization. CCD1 for imaging the sample surface and CCD2 for spectrally resolving of the QD emission. The polarizers, POL, are used for the suppression of the laser and enabling resonant spectroscopy on single QD. The dotted lines show tiltable optical elements, solid lines presents non-moveable components and the red arrows indicating the possible connections for the SMF.

Elements of Optical Setup

Item	*Description*	*Manufacturer, Product*
SMF1,2	single mode fiber defines the excitation path	Thorlabs, P3-830A-FC5
SMF3,4	single mode fiber defines the detection path	Thorlabs, P3-830A-FC5
FC1,2	fiber couplers f = 18.4 mm, NA = 0.15	Thorlabs aspheric lenses C280TME-B
BS	beam-splitter; non-polarizing, 50:50	Thorlabs BS017
POL1,2	linear polarizer	Thorlabs LPVIS050 (sodium-silicate glass)
FEL780/800	780/800 nm longpass filter	Thorlabs FEL780/FEL800
PM	Powermeter	Thorlabs powermeter PM100D
WM	wavemeter, accuracy = 0.005 nm	Coherent WaveMaster Wavelength Meter
PBS	pellicle beam splitter, (R:T) 8:92	Thorlabs BP108
SPEC	spectrometer: f-number = 6.5, f = 500 mm, $\frac{\Delta\lambda}{\Delta x}$ = 1.52 nm/mm	Princeton Instruments SP2500
CCD1	CCD camera, imaging of the sample surface	
CCD2	front illuminated, liquid cooled CCD	Princeton Instruments PyLoN 100F
MO	50x microscope objective, NA = 0.55, f = 4mm	Nikon CF Plan 50X, EPI, mounted on a z translation stage with step motor

Table 5.1: List of the most important optical components.

important values of the optical setup

values	*quantity*
collection efficiency optical setup	$5 \cdot 10^{-7}$ - $3 \cdot 10^{-5}$
coupling efficiency SMF 1	1/30 - 1/20 (2 - 6 mW) for DL1/2
coupling efficiency SMF 3	35 - 50% for DL2
operational current DL1/2	150 mA
applied power to probe samples	0.5 - 10 μW
optical density filterwheel	6:0, 1: 0.1, 2: 0.2,3: 0.5, 4: 1.0, 5: 2.0
suppression for RF	$1.0 \cdot 10^6$

Table 5.2: List of important values for running the optical setup

This setup is mainly used for fast[1] (non-resonant) characterization measurements in order to get an overview of the different energy states which reveals the central-emission wavelength λ_c, the density (how many QDs are within the focus) as well as the brightness of the QD (saturation intensity), shown in figure 5.2, the purity of the sample (shape of GaAs and wetting layer peaks), the charging of the QD (functionality of gate) and also light matter interaction enhancement/ suppression phenomena.

The optical path was set up using fibers. Fibers are flexible and allow guiding the light over different paths by just connecting them with each other without realigning the system. Furthermore, single mode fibers (SMF) support only one mode which is of great importance for resonant fluorescence measurements. A flow cryostat is used that allows uncomplicated exchange of the samples. To guarantee high stability, the cryostat is mounted vertically on a 25 kg aluminium block. Furthermore, the flow cryostat is installed directly at the back of the non-polarizing beam splitter. This geometry allows for a direct optical access of the sample, so that the laser beam retains

[1] allows for a swift change of samples and short alignment procedure

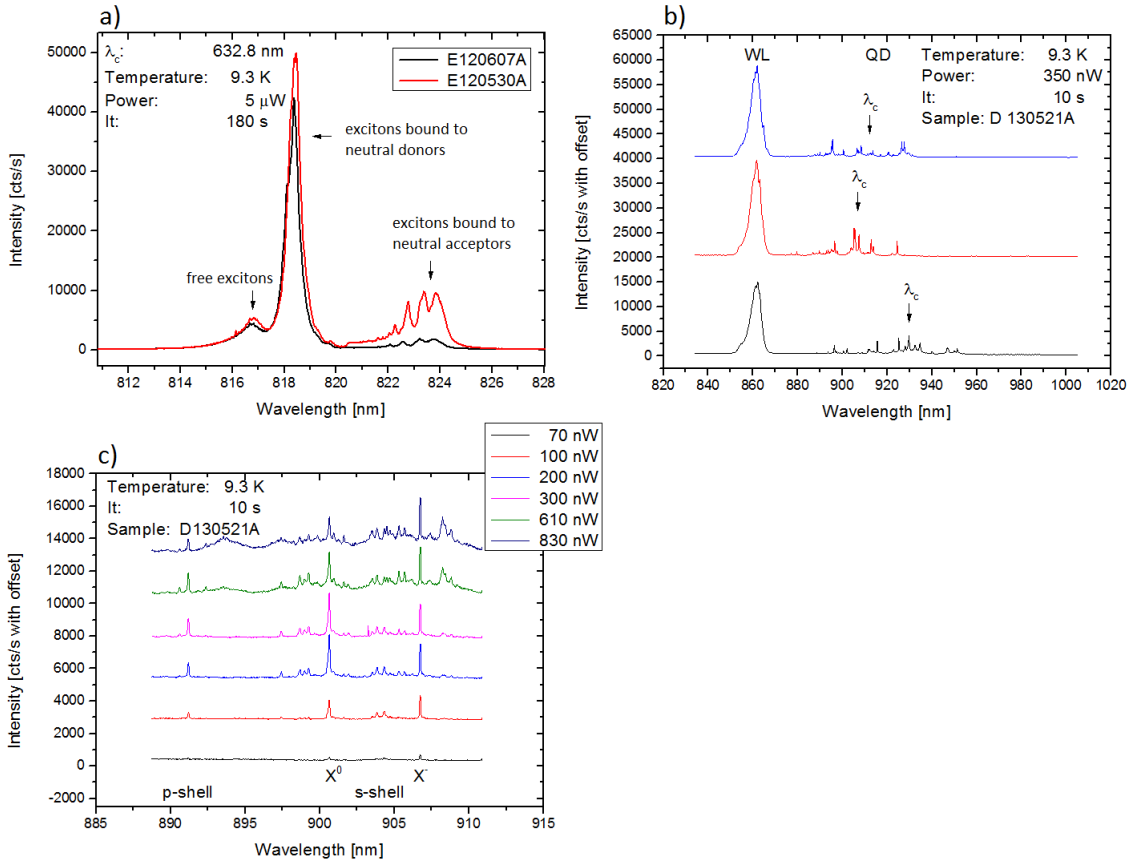

Figure 5.2: a) PL spectra taken from two different GaAs probes, the main peak at 818 nm is surrounded by smaller peaks, indication for impurity states. b) the three PL spectra are from the sample D130521A and differ by about 1.5 μm. Showing the density difference and emission properties (λ_c = central wavelength emission) of the QD (3-4) in the focus (inhomogenous broadening). c) Intensity measurement for D130521A, the X^0 and X^- peaks are clearly visible, at higher pumping power (over 200 nW) a peak at higher energy emerges, indicating for p-shell pumping.

its polarization state[2], see figure 5.1. In the following sections the above mentioned values and optical parts are discussed in more detail.

5.2 Gaussian Beam Optics

The assumption of a Gaussian beam profile (TEM_{00} - mode) is the simplest and yet accurate approach to describe the propagation and focusability of most lasers[3]. For microscopic studies the knowledge of the diffraction limited focal spot is of great importance because it defines the obtainable spatial resolution for optimally adjusted optics and ideal Gaussian beam ($M^2 = 1$[4]):

$$d_{FWHM} = 2 \cdot \omega_0 = K_{FWHM} \frac{\lambda}{2NA}. \tag{5.1}$$

The beam waist ω_0 (the radius of the beam in the focus) and the corresponding diffraction limited spot size d_{FWHM} with $FWHM$ = full width at half maximum, depends mainly on three parameters: the numerical aperture ($NA = n \sin \alpha$, with is the half-angle of the maximum cone of light that can enter or exit the lens) of the focusing objective, the wavelength of the applied light, λ, and the correction factor K(T) (figure 5.3) that incorporates the effects of the intensity distribution illuminating the lens[5] and the ratio of the illuminated area to the area of the focusing lens, the truncation ratio $T = \frac{2\omega}{d_{obj}}$:

where K_{FWHM} can be determined by the phenomenological formula

$$K_{FWHM} = 1.029 + \frac{0.7125}{(T - 0.2161)^{2.179}} - \frac{0.6445}{(T - 0.2161)^{2.221}}. \tag{5.2}$$

[2]With this configuration it is possible to get suppression factors up to $1.6 \cdot 10^6$, in comparison to 10^3, where the cryostat was installed directly on the optical table and the light had to be guided to the sample surface using additional mirrors causing instabilities in the polarization state.

[3]Laserdiodes have usually a non-optimal intensity profile composed of several modes, but can be improved to get a higher M^2 by the coupling into a single mode fiber to a Gaussian beam shape.

[4]beam quality factor, since its value can be used to quantify the degree of variation the actual beam is from such an ideal beam.

[5]A uniformly illuminated lens creates an Airy disc intensity profile in the focus. By illuminating the lens such that the radius of the lens equals the $1/e^2$ beam waist of the impinging Gaussian beam, the intensity distribution in the focal plane is Gaussian [28].

It follows that to get high spatial resolution, a high NA and a small K value is needed.
The NA is restricted to be less than 1 (surrounding medium air). Additionally objectives with high NA have a smaller working distance (distance between the objective and focal plane). In our configuration the working distance cannot be shorter than 5 mm (distance from the window of the cryostat to the sample surface), thus the working distance supported by the objective should be at least 6 mm so that the objective comes not into to close contact with the cryostat. A good choice for the objective is the CF EPI Plan from Nikon with a $NA = 0.55$ and a working distance of 8.7 mm.
From figure 5.3 follows, that K is strongly decreasing in the range for T from 0 to 1, and that for $T > 1$ the curve is only slightly decreasing; converging to the limit 1.029. Although K_{FWHM} will decrease for increasing T, leads to high losses by overfilling the microscope objective. Thus the best value is therefore given for $T = 1$. For our system we can measure a truncation ratio of $T = 4.9/4.4 = 1.11$[6], which means that we are losing some of the excitation power. However, this is not of great importance because we only need some nW up to few μW. The overall coupling into the microscope objective is measured to be 56% (transmission grade and overfilling of the objective).
Altogether this corresponds to a focal spot diameter of 0.8 μm and 1.0 μm depending on the central wavelength of the excitation laser, 785 nm respectively 950 nm.

The focal depth $\pm z_f$ is a measure for the placement tolerance of the MO and describes per definition the range in which the beam waist varies about maximally 5 %,

$$z_f = 1.28 \frac{\lambda}{NA^2}. \tag{5.3}$$

The focal depth depends linearly on the wavelength and decreases quadratically with the NA of the objective, a high NA leads not only to a small focus point but also to a reduced focal depth. For our objective and $\lambda = 980$ nm the focal depth is 8 μm; for the depth-adjustment of the microscope objective (MO), is therefore a screw with micrometer sensitivity needed.

[6]The beam diameter, 4.9 mm, is appromximatively determined with a powermeter and an aperture, the aperture is so far closed until only 86 % of the initial intensity is detected.

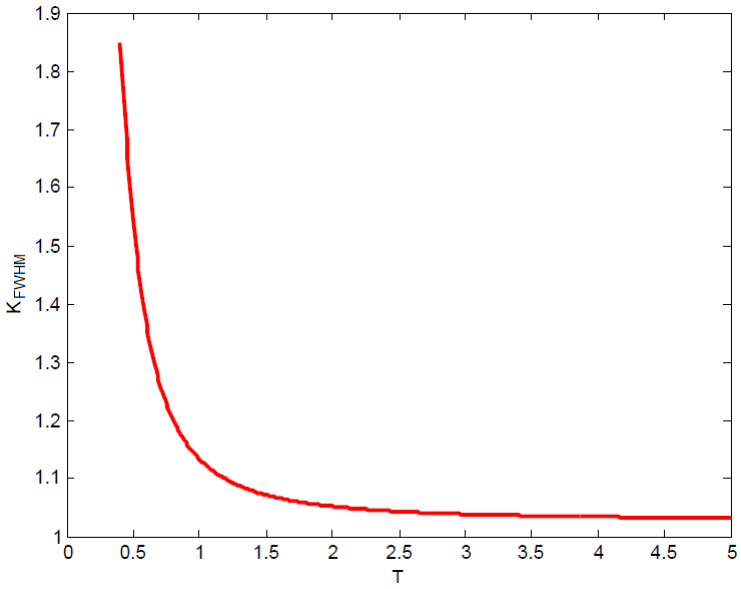

Figure 5.3: K values as a function of the truncation ratio T.

5.3 Confocal Microscopy

The confocal feature, i.e., that only light can be detected inside a diffraction limited focus (formula: 5.2) of the microscope objective (signal), leads to strong suppression of light outside this area (noise) and with it to a better signal to noise ratio[1].

For single QD spectroscopy the density must normally be strongly reduced (normal QD densities are around $10^{10} - 10^{11}$ cm^{-2}) by special processing of the sample with shadow masks or mesa etching in order to reduce the light contributions from QD outside the focus. The confocal approach is therefore a convenient way to select a small area of interest from the QD ensemble without further actions. A drawback of the confocal microscopy is that the

[1] Confocal microscopy also slightly improves the lateral resolution: $0.4\frac{\lambda}{NA}$ compared to: $0.56\frac{\lambda}{NA}$ for T = 1 (see equation 5.2) and enables for real axial resolution compared to just the depth of focus which is usually given as the axial distance between just blurred images. But this enhancement in resolution depends on the pinhole and the best SNR value is obtained if the pinhole diameter equals an airy unit: $PH = 1AU := \frac{1.22\sqrt{2}\frac{\lambda_{em}\lambda_{exc}}{\sqrt{\lambda_{em}^2+\lambda_{exc}^2}}}{NA}$ with λ_{em} and λ_{exc} the emission and excitation wavelength [38]. For smaller pinhole radii the resolution improves only slightly but the signal diminishes and vice versa. In our case we have a pinhole diameter of 4.6 μm that equals 2.5 AU; the lateral resolution is therefore given by the gaussian optics. Further informations can be looked up in [39] and a quantitative description is given in [40].

pointwise collection of light does not give any spatial information, which can only be obtained by scanning over the surface. But this plays only a minor role, because scanning is only used in finding a suitable QD. As soon as an appropriate QD is found, the QD remains in the focus until the spectral analysis of the focused QD is done.

A confocal microscope can be realised by putting a pinhole in the image plane of the objective. The objective in our case consists of two lenses, that are aligned such that the focal area of one lens, the object lens, is imaged by the second lens, the ocular lens onto a pinhole. The pinhole in our setup is a single mode fiber with a core radius of 4.6 μm and an NA of 0.12. Only the light within the cone bounded by the angle $\theta_a = \arcsin NA/n_0$ can be coupled into the fiber and contribute to the detectable signal [28]. As explained the usage of fiber has several advantages, one drawback however is a decrease in the detectable signal because normally only 40% of the original intensity can be properly coupled into a single mode fiber.

5.3.1 Imaging and Magnification

The supported magnification of our microscope objective, focal length $f_1 = 4$ mm, is M = 50x. To get a sharp and correctly magnified image on CCD1[7] from the MO an ocular lens, focal length $f_2 = 200$ mm, is needed that matches the following formula: $M = \frac{n_1}{n_2}\frac{f_2}{f_1}$ [40].

The microscope objective in use is an infinity corrected objective[8]. This has two advantages:
First, the installation of further optical components such as polarizer, beam splitters and filters have hardly any effect on the light path in comparison with a convergent beam. Second, the distance between the MO and the ocular lens does not have any influence on the image quality of the ocular lens which allows for an independent adjustment of the MO.

[7] CCD1 is used for imaging of the laser spot on the sample (checking for proper coupling), PL signal of QDs and orientation on the sample

[8] this means that if the investigated object is located in the focal plane of the MO the outgoing light of the objective is collimated.

5.3.2 F-number matching

As seen from the resolving power (5.5.3) a spectrometer works best for a completely filled grating. To fulfill this condition the f-number of the coupling lens and the spectrometer should match.

This assures that the grating will be completely illuminated and therefore the highest resolving power is achieved.

The f-number is the ratio of the focal length f to the illuminated area on the focusing optic [41]:

$$F/number = \frac{f}{d} = \frac{1}{2\sin\alpha}. \tag{5.4}$$

With α the half opening angle of the maximum cone of light that can enter the lens. Small f-numbers have steeply-angled rays and high f-numbers corresponds to slightly divergent beams. If the f-number of two optics cannot be matched its advisable to use a f-number for the coupling lens that is higher compared to the other. Thus the other optics is underfilled, but no light is lost. Overfilling would not only lead to a loss of signal but also to stray light. The used spectrometer has an f-number of 6.5. The lens used to couple the freespace path into the spectrometer has a focal length of 35 mm, with a beam diameter of 4.9 mm. The f-number is thus 7.1 and underfills the grating.
Interestingly (see figure 5.4) the effect of the application of a non-optimal lens does not have such a big impact.

5.4 Non-resonant μPL

The μPL-measurements and the resonant spectroscopy (see 7.2) studies on single QD have been carried out on an home built fiber-based, confocal working optical setup. Laser light and photons collected from the system are transported via single-mode fibers. As a result, the excitation and detection paths form an independent unit, furthermore it allows for an easy check of the quality of the alignment, discussed in A. An overview of the optical setup can be seen in the graphic 5.1.

The system consists of four lasers:
An external-cavity diode laser for the resonant excitation of the QD states, TL (short for tunable laser). For this purpose its essential to have a narrow

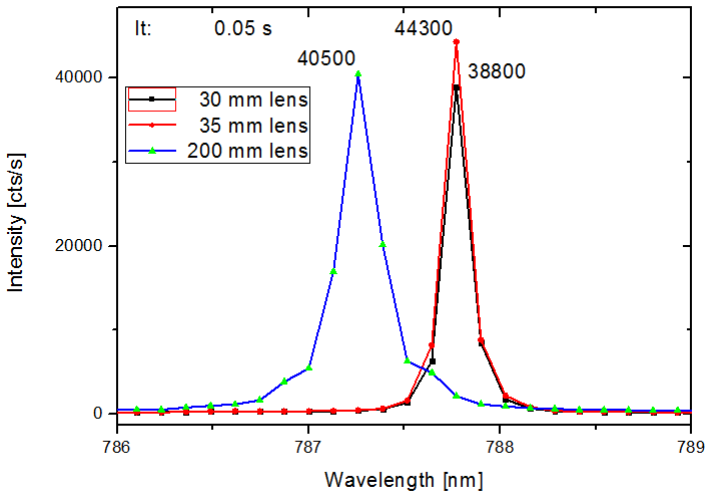

Figure 5.4: Three different lenses have been tested to see the difference in resolution and intensity of the signal. The 35 mm lens and 200 mm lens underfill both the grating, but the 30 mm lens should slightly overfill the grating. This can be seen by the reduction of the detected events from over 40000 to 38000. The resolution is lowest for the 200 mm lens, which follows from its lowest f-number and thus the smallest illuminated area on the grating. The best choice is thus the 35 mm lens. The difference in the spectral position of the 200 mm lens compared to the 30/35 mm lens is due to non-matched adjustment.

bandwidth laser that is tunable in a mode-hop free manner. The laser in use has a fiber-dock that allows for a direct coupling into the excitation path with the fiber SMF2 (more details given in 5.5.1). An AlGaAs infrared diode laser, abbreviated as DL1 is used for the non-resonant excitation with a lasing wavelength of 786 nm. A laser diode, short DL2, for the alignment of the optics especially the focii on the emission wavelength of the QD with a lasing wavelength of 981 nm. Both the alignment and non-resonant excitation diode lasers are connected with a laser diode driver LDC205C from Thorlabs. They are operating at 150 mA which corresponds to an output power of approximatively 60 mW. The beam profiles of these lasers are strongly divergent and elliptical, so they are mounted in a collimation tube and are coupled into the single mode fiber SMF1 over an aspheric lens L1 via the mirrors M1 and M2 respectively M3 and M4. Additionally, a helium neon laser, HeNe, is used for the coarse alignment of the optics as it is visible with a wavelength of 632.8 nm. The HeNe is coupled into SMF1 with the mirrors M5 and M6.

The coupling into the single-mode fiber changes the elliptical, multimode beam of the diode lasers considerably, because only Gaussian like modes are supported by this kind of waveguide so that, the beam profile is Gaussian at the output of the fiber [42]. SMF1 is connected with another fiber SMF2 over a fibercoupler FC1. This approach allows for a swift change of the beam path without disturbing the alignment, which is likely to happen if the fiber had to be disconnected at the fiber port. The output wavelength is controlled by an optical wavelength meter WM, whose sensor is installed behind the exit port of fiber SMF2. A negligible part of the excitation light is coupled into the wavemeter for measuring the wavelength with an accuracy down to a few picometer. To control the excitation power, a double filter wheel is placed in the optical path. Each filter wheel is loaded with 0.0, 0.1, 0.2, 0.5, 1.0, 2.0 absorptive optical density filters. Additionally, DL1 can be continously damped with a continously variable neutral density filter CVNDF. The light at the exit of the fiber is collimated by CL2 and guided by M7 and M8 via a beam splitter BS[9] where the transmitted light is blocked and the reflected light goes through the MO onto the sample surface that is mounted in a flow cryostat (see 5.5.2). The luminescense is collected with the same objective and transmitted by the BS towards a pellicle beam splitter PBS. The pellicle beam splitter sends 8% to CCD1. In front of CCD1 is a tiltable longpass filter FEL800 mounted to suppress the laser from the signal. The PL signal is then imaged by the ocular lens L3 onto the camera chip with a total magnification of 50x. The remaining 92% passes two tiltable longpass filters FEL780, FEL800 to spectrally filter the reflected laser light form the PL signal. After these filters it is possible to choose between a freespace or fiber-based detection path.

For the fiber-based detection path, the light is coupled by M9 and M10 into SMF3. SMF3 is connected with SMF4 over a fibercoupler FC2. SMF4 is fixed on a moveable U-Bench for an appropriate coupling of the signal into the spectrometer. The light at the output is collimated with CL3 and focused with CL4. The freespace detection path leads over M11, M12 and M13 to the second entrance of the spectrometer and is focused onto the entrance slit with L4. The proper alignment is done with M12 and M13.

[9] To enhance the stability of the system the BS is mounted in such a way that the more sensitive optical path lies in the direction of transmission. Thus a small tilt of the BS leads to a change of direction for the reflected beam but only to a small offset for the transmitted beam.

5.5 Resonant Spectroscopy

For resonant excitation the same confocal setup as for PL experiments is used. Thus, the reflected light is detected. In order to suppress the back-reflected laser light, which is resonant with the electronic transition from the sample, the so called crossed polarization technique is used:

For resonant spectroscopy, the sample is excited with a linearly polarized beam by using the polarization filter POL1. The photons from the two level system and laser light are collected with the MO. In the detection path the second polarizer POL2 is oriented perpendicularly to the laser polarization. With this arrangement it is possible to get a suppression factor of the laser of up to $1.6 \cdot 10^6$. Such high suppression factors can only be obtained by careful alignment of the two polarizers[10] and if the polarization of the laser light coincides with the crystal axis of the BS, otherwise the measured suppression is about two orders worse because of the elliptical polarization of the beam. Furthermore the polarization suppression is extremely sensitive on instabilities of the cryostat and additional optics after POL1. They can lead to polarizations deviating from linear, and hence reduce the suppression quality significantly. Another improvement in the suppression of the laser is the use of a SMF in the detection path, because the initial Gaussian mode and polarization state of the laser being reflected and passed through several lenses of the MO gathers components of higher-order modes. Since these modes propagate differently within the detection path (MO, BS, M), they are encountering different environments and with it the polarization varies independently form the other modes (private communication Dr. Andreas Reinhard and Meinrad Sidler). If this beam is then coupled into a SMF in a mode matched manner, the fundamental mode (Gaussian mode) will be cleaned from the higher order modes (figure 5.5). This fiber purification step improves the suppression by about one order of magnitude in comparison to the freespace detection scheme [11].

[10]The best suppression was achieved by repeating the alignment of the polarizer: After the first alignment it is good to wait until the suppression of the laser got into its steady state, most often it increases by up to two orders and than suppress the laser again until the laser stays suppressed on a high level.

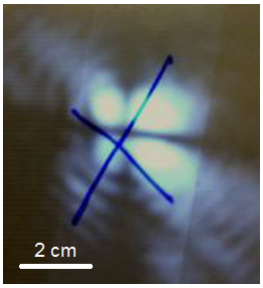

Figure 5.5: The CCD image of the suppressed laser. The Gaussian mode is not anymore visible on the CCD (center of the beam), but the higher order modes which form a cloverleaf around the center.

5.5.1 Tunable Laser

As excitation laser for the resonant excitation of the QD, an external cavity diode laser, in short ECPL, DLPro100 from Toptica, is used. The laser is connected with a D110 - Diode laser supply and control rack.

The core of the tunable diode lasers is its resonator. The resonator is built up by a reflection grating that reflects the $m = 1$ order back into the lasing medium and diodes back facet.
The length of the cavity as well as the feedback light is defined by the angular position of the grating. The length of a cavity determines the longitudinal mode structure, the feedback light the light with the least loss and the coincidence of both set the lasing mode. Both of them can be shifted by tilting the grating and with it tuning the output $m = 0$ of the laser. As long as the change of the incident angle and the change of the resonator length is synchronized no mode hopping appears, otherwise a new mode will have the least loss and starts to lase which leads to an abrupt change in emission wavelength [43, 44]

The grating allows for a coarse, mechanical adjustment using an external micrometer screw; the tunable range and the corresponding output power can be seen on the left side in figure 5.6. Fine tuning is done by applying a voltage over a piezo actuator. During the fine tuning process mode-hopping was observed (figure 5.6).

The TL can also be tuned by varying the temperature range ($19° - 25°$) and the diode current ($87mA - 130mA$). The temperature has a direct influence on the refractive index and with it, the length of the cavity, furthermore the energy spacing of the lasing niveaux change by a change of

temperature, which shifts the gain profile. A similar effect is caused by a change of the diode current, where the refractive index changes because of the new charge carrier distribution and the energy spacing by the applied voltage. As the alteration of the cavity length and the shift in the gain profile is not synchronized in both cases, mode hopping is very likely to occur [45]. Because of that, the laser is only tuned by the change of the grating angle during the experiments .

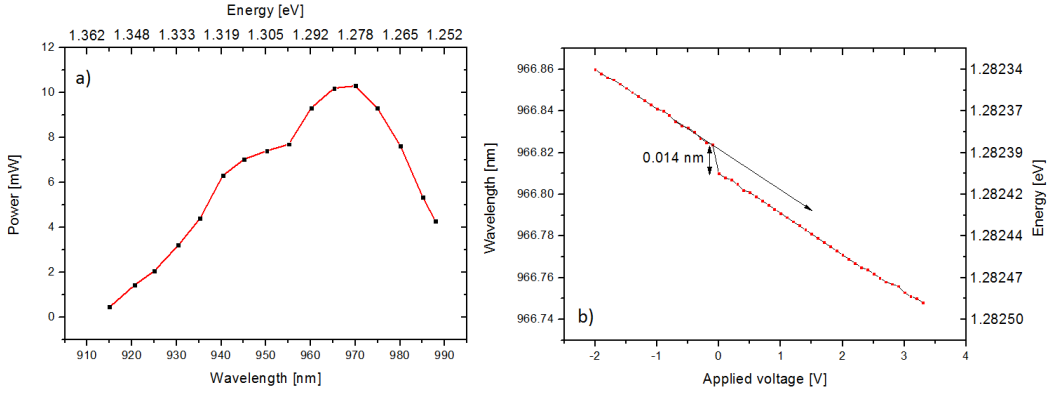

Figure 5.6: a) Tuning range and output power for the tunable laser. b) Mode hop during a fine adjustment. Mode hopping phenomena are only observed by scanning over large ranges (over 2 V).

5.5.2 Cryogenics

To observe narrow emission lines of a single QD all the experiments are conducted at cryogenic temperature around 9 K. For higher temperatures the emission is red shifted and broadenend due to higher phonon-scattering rates; at 50 K thermal relaxation dominates over the optical QD recombination [11].

The low temperature regime can be obtained by the usage of a liquid-helium flow cryostat. Our system is a flow cryostat from Oxford Instruments: Microstat Hires2. The cryostat top cover is custom made and facilitates the usage of nanopositioning units that also work at croygenic temperatures down to 0.1 K, called attocubes. The attocube enables for a reproducible scan and an accurate positioning of the QD into the focal spot. The common stability of the attocubes and cryostat is high enough that even resonant spectroscopy measurements over a period of more than 5 h can be carried

out. A 0.5 mm spectrosil B window on top of the samples enables for optical access.

To operate a continous flow cryostat the following components are needed: the transfer line, the cryostat (cryostat), the turbomolecular pump and a temperature controller. Before the cryostat is cooled down the air has to be pumped out to minimize thermal conduction between the sample and the outer wall of the cryostat; normally $10 - 20 \cdot 10^{-6}$ mbar. This vacuum is obtained by the usage of a turbomolecular pump from Pfeiffer Vacuum for a pump duration of around 30 min. The operation of the cryostat is based on a continuous flow of liquid helum through the transfer line that allows for the adjustment of the helium throughput by a needle valve. The helium is sent into a capillary system and flows into the heat exchanger where it is vaporized and removes the heat from the sample space [46]. The gaseous helium returns over the transfer line into the helium recovery system. After a thermalization process of around one hour the cryostat reaches a temperature of around 9.3 K. After this, the needle valve is completely closed and slightly reopen to maintain the temperature and reducing the helium throughput. At this temperature the alignment of the optical system and experiments can be carried out. The helium consumption during a normal experiment is estimated to be around 2.5 l/h.

The wiring of the cryostat is shown in figure 5.7. The top- and backgate of the semiconductor chip are connected with the DAQ-card and is controlled by software written by Dr. Martin Kroner. The software enables for a synchronization of spectrometer and DAQ card and with it the possibility to do gatesweep measurements. The photodiode is underneath the sample holder and its signal can be directly read out by a voltmeter. The attocubes are connected with the positioning controller. The attocubes can be translated over a full range of 3 mm with a maximal resolution of 10 nm at 4 K. The temperature sensor is in contact with the attocubes and determines their temperature. Thus, the displayed temperature is likely to deviate from the real value. The exact amount of the temperature deviation was not determined in this thesis, but due to linewidth measurements of the QD excitons it is believed that the deviation could be as big as 10 K (section 7.2).

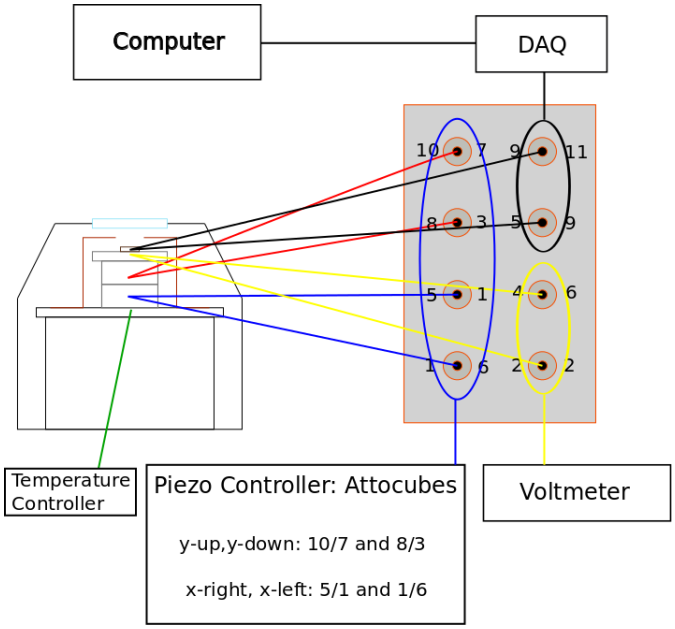

Figure 5.7: The blue and red wire are for the control of the attocubes, the yellow for the readout of the photodiode and the black wire for the voltage control of the heterostructure. All these wires are connected with the respective controler: piezo-controler, voltmeter and DAQ via box. The temperature sensor is directly connected with the temperature controler as shown.

5.5.3 Spectrometer

In the optical setup a spectrometer of Princeton Instruments, Acton SP-2500i, is used. It is an imaging spectrograph in Czerny-Turner configuration. Imaging spectrograph means that that every point at the entrance slit is imaged, in our case 1:1, on the exit slit. In the figure 5.1 the ray path for a general Czerny-Turner spectrograph is shown: The light enters the spectrometer by one of the two entrance slits. Both of them were used, the front entrance slit for the free space detection, and the side entrance slit for the fiber collection path. The only difference between the two entrances is that the side entrance is indirectly imaged over a plane mirror onto the first curved mirror (collimating mirror) with a focal length of 500 mm (distance from the entrance slit to the mirror). After this mirror the light is collimated and directed towards the gratings, which are mounted on a turret and can be easily changed and adjusted for the interesting wavelength range by the software Winspec. The turret allows for the mounting of three different gratings of the size 68 mm x 68 mm. The dispersive element of our

spectrometer is a blazed holographic respcectively ruled plane grating: 1500 $\frac{l}{mm}$, blazing angle 850 nm and 300 $\frac{l}{mm}$ blazing angle 750 nm. The grating spectrally decomposes the light and reflects it to the second mirror (focusing mirror) with the same focal length. The second mirror focuses the light onto CCD2. The used detector is from Princeton Instruments, consists of 1340 x 100 square pixels with a size of 20 μm x 20 μm (total size: 26.8 mm x 2 mm) and is cooled down to around -120° C using liquid nitrogen to eliminate thermally excited charge carriers and thus to a considerable reduction of the dark current.

Resolution

The reciprocal linear dispersion value is, along side the resolution power, the most important feature of a dispersive working spectrometer

$$\frac{\Delta\lambda}{\Delta x} = \frac{d\cos\beta}{fm} \overbrace{\approx}^{\cos\beta<20^\circ} \frac{d}{fm}. \tag{5.5}$$

With β the angle of diffraction, f the focal length of the spectrometer, d the grating constant and m the order of diffraction. In the last step of the reciprocal linear dispersion formula it is assumed that the diffraction angle is smaller than 20°.

The resolution power of a grating, $R = \frac{\lambda}{\Delta\lambda}$, describes its power to resolve two adjacent spectral lines λ and $\lambda + \Delta\lambda$. The maximum possible resolving power of a grating, neglecting aberrations, assuming a perfect grating (no defects such as dust) and for an infinitly small entrance slit width can be shown to have the following form

$$R = mN \tag{5.6}$$

and depends solely on the order of diffraction and the total number of illuminated grooves. In first order ($m = 1$) one gets for the 1500 l/mm and 300 l/mm grating: $R = 102000$ and $R = 20400$. Assuming a central wavelength of 980 nm, it should be theortically possible to distinguish between two spectral lines which differ by $\Delta\lambda = 0.01$ nm and $\Delta\lambda = 0.05$ nm, respectively.

The resolution $\Delta\lambda$ of the detector can be calculated by the usage of the linear reciprocal dispersion formula 5.5 times the width of a pixel. The width of one pixel is 20 μm and therefore the resolution of the detector is 0.026 nm

(1500 $\frac{l}{mm}$) and 0.13 nm (300 $\frac{l}{mm}$). It can be clearly seen that the resolution is to first order limited by the detector which is roughly three times smaller than the resolution determined by the grating.
The measured resolution of the spectrometer (see figure: 5.8) is fairly close to the calculated values above despite that many effects such as diffraction or the width of the entrance slit width have been neglected. A more sophisticated formula shows the most important dependencies of the spectral resolution [47]:

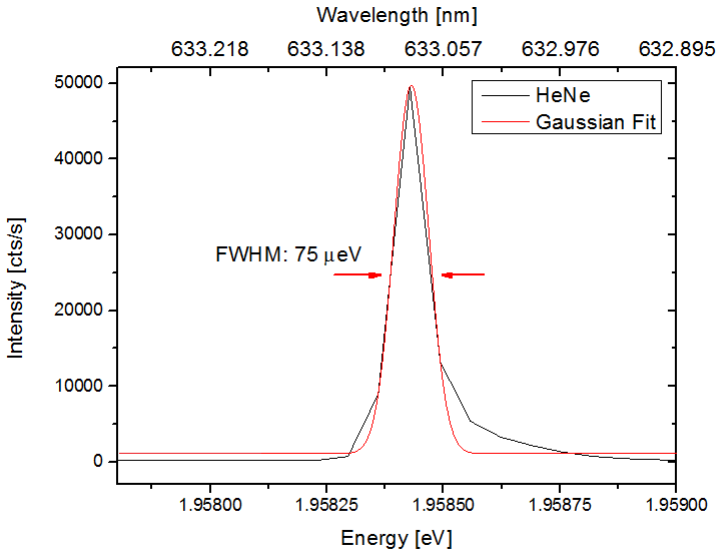

Figure 5.8: To measure the spectral resolution capability of the spectrometer the FWHM of the Gaussian fit of the HeNe laser was determined. By optimal adjustment (optics and slit) a FWHM of 0.029 nm (75 μeV) can be achieved. This resolution is clearly above the assumed FWHM of spectral width of the QD excitons (around 1 μeV).

$$R = \frac{\lambda f m}{b g \cos\beta} \qquad \begin{cases} .\beta & : \text{ angle of diffraction} \\ b & : \text{ entrance slit width} \\ f & : \text{ focal length} \\ d & : \text{ grating constant} \end{cases} \tag{5.7}$$

It can be seen from the formula above, that a narrower slit is preferable for best wavelength resolution. However, it is obvious that the narrower the slit gets, the radiant power reaching the detector will decrease gradually and

deteriorates the detection ability. Considering the fact that the brightness of a single QD is rather low and the collection efficiency is poor it is preferable to maximize on the intensity of the signal rather than its resolution.

Chapter 6

Samples

Here we want to present the field-effect structure and micropillar sample used to test the capabilities of the optical setup. The section on the field-effect structure 6.1 is divided into two subsections 6.1.1 and 6.1.2. The first subsection describes the growth and fabrication of the heterostructure. The second subsection discusses the control mechanism to load single electrons into the QD and the tuning of the QD emission.
Section 6.2 describes the geometry of the micropillar and the temperature tuning to bring the QD into resonance with the cavity modes.

6.1 Field-Effect device

6.1.1 Sample Growth and Preparation

The growth of the planar layers and the QD was made by molecular beam epitaxy (MBE). MBE is a widespread semicondcutor fabrication technique that gives full control over the deposition of atomically thin layers. The materials used are ultra pure (99.999999% pure) and the depostion runs in a ultra high vacuum (10^{-11} mbar) to minimize defects and impurities [48]. They are stored in diffusion cells that can be independently heated and closed to steer the atomic flux onto the wafer, a [100] GaAs-substrate. The GaAs-substrate on which the heterostructure is grown is mounted on a rotating holder for a homogenous covering of the surface with the incoming atoms. The substrate is not perfectly flat and shows several defects, mainly due to the mechanical fabrication steps, this can alter the electronic and optical properties of the following structures. To reduce the surface roughness

and to obtain a clean surface a GaAs buffer layer is deposited (private communication Dr. Stumpf and Dr. Fält). On top of the GaAs buffer is the DBR (distributed Bragg reflector). The DBR consist of 29 mirror pairs of quarter-wavelength thick layers of GaAs and AlAs, followed by a highly n-doped[1] layer acting as the back contact of the device and an intrinsic 35 nm GaAs layer, the tunnel barrier. Through this barrier electrons can tunnel from the back contact into the QD and vice versa. The next layer is the QD layer, where the GaAs material is covered with InAs, which leads to the formation of InAs islands. This step is different from the other steps because during the growth of the QD the rotation of the wafer is stopped. If this is switched off there are regions where more material is deposited, that means that the critical layer thickness is reached earlier, and with it the growth of QD.

The QD are grown in the partially covered island mode (private communication with Dr. Stefan Fält), in which, the growth sequence during the capping of the InAs islands with GaAs is interrupted. During the interruption phase indium diffuses out and leads to a flattened island (height $\approx$ 2 - 3 nm and diameter $\approx$ 20 nm, compare with figure 3.2). The smaller thickness of the QD reduces the emission from 1100 nm to 950 nm[2]. Then another GaAs layer, the capping layer is grown. The last two steps are the deposition of the AlGaAs blocking barrier, which reduces the leak current and the final GaAs layer protects the aluminium in the blocking layer for oxidation.

After the growth process the individual samples must be prepared. To get a sample ready for experiments post growth processes are needed which are explained in the following: Because the samples for the experiments are limited in size (5 mm x 3.5 mm) the useful pieces have to be cut out of the heterostructure. For a heterostructure with a DBR only a small area can be used for further investigations. This comes from the fact that the grown DBR structure is not perfectly flat but exhibits for the different layers different thicknesses (radial symmetrical). The central layers are thicker than the one on the outside. Thus only on a circle around the center the DBR-layers has the correct thickness. Additionally, the growth gradient of

[1] the type of doping defines the kind of carriers which tunnel in and out of the QD: for p-doping holes, for n-doping electrons.

[2] 1100 nm is not accessible for the Si-Detector in use because of a low quantum efficiency and 950 nm is well covered by the Si-detector.

the QD must be low enough for single QD spectroscopy. Only the regions were the thickness and density matches can be further used.
To know where the good parts are located a PL-map of the structure is made (see 6.1). From this map the best region is chosen for the experiments. In our case of single dot spectroscopy the transition region from "milky blue" to "dark blue" can be used.

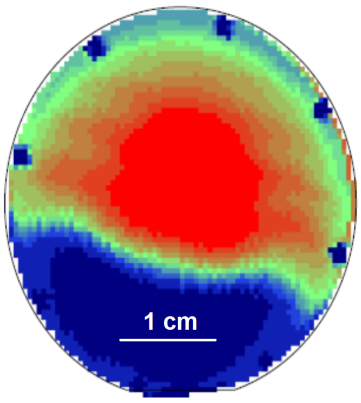

Figure 6.1: The PL map shows the integrated PL peak intensity at room temperature for an emission wavelength between 900 and 1200 nm of the field-effect structure, ES1795. The red parts indicates high QD density regions, dark blue no QD to very low density part.

That region is splitted off and cleaved to the size of the later used samples. To get a working field-effect structure the n-doped layer must be made accessible and the topgate has to be fabricated that the final sample can be connected with the source voltage. To contact the n-doped layer a channel from top of the field-effect structure through all the layers is made. This contact is realised by the diffusion of indium. Because indium oxidizes swiflty under normal condtions it must be cleaned. Therefore the indium is cut first into small cubes (≈ 1 mm^3) and the oxidized surface is cut off by a sharp razor knife. Two clean indium pieces are then put in the corners[3] of the surface. Two contacts are needed to check if the connection to the backgate was succesful. For the diffusion of the indium the sample is heated up in 3 steps up to $450°C$, this temperature is then held constant for 7 minutes. The whole process take place in an conventional oven filled with forming gas. Afterwards the sample is cooled to room temperature and the resistance is tested. The measured resistances are around $100 - 500\ \Omega$.

[3]because these areas cannot be used anymore, the indium flakes are put in regions where its known in advance that the density is too high/low.

The topgate consists of a 2 nm thick titan stickinglayer and a $4-6$ nm thick gold layer, because gold is an excellent conductor. The few nanometer thick topgate is semitransparent for the QD emission and the excitation laser. It is deposited in an evaporation system under high vacuum (10^{-5} mbar). This system facilitates the deposition with an accuracy of less than 1 nm and is controlled by a computer, where the deposition rate and the layer thickness can be supervised. The topgate is defined by a shadow mask in a form of a key. By the placement of the shadow mask attention must be paid, that there is enough space between topgate and the indium channels, otherwise leak currents or even a short circuit can result. The material is stored in a crucible and heated by a 50 kV cathode beam that is guided by a magnetic field on a circular trajectory to ensure a homogenous heating.

The complete samples are fixed on copper plates to be mountable on the top of the nanopositioning units (see 5.5.2) inside the cryostat. The copper plates have a hole that makes it possible to localize the current position of the laser spot on the sample at a closed cryostat. The structures are transparent for laser light with photon energies below the wetting layer states ($E_{wl} \approx 1.45$ eV). Below the sample a photodiode is installed and connected with a multimeter for the read out of the current, if the laser is off the hole no current will flow and vice versa. On top of the copper plates sits a soldering pad. The pad is fixed with epoxy. The sample is glued on top of the copper plate with varnish which is electrical insulating and adhesive at cryogenic temperatures. Finally the connections between the sample, pad and the cryostat are made. The pad is connected with the output channel of the cryostat and the back- and topgate is each connected by a thin copper wire with a different channel over the pad.

6.1.2 Functionality of the Field-Effect Device and Quantum-confined Stark Effect

The complete heterostructure of ES1795 can be seen in figure 6.3 and a schematic graphic of the bandstructre bending is shown in 6.4. From figure 6.4 it is clearly visible that the high doping in the back contact ties the Fermi-energy to the Si-dopant levels and that the slope of the conduction- and valence band between the back- and topgate is set due to the metal-

semicondcutor contact (Schottky-diode: V_s about 0.62 V) and the applied voltage V_g. With the application of a negative voltage (positive voltage) the bandenergies are shifted up (down) by

$$\phi(z) = -e\frac{z}{b}V_g, \tag{6.1}$$

with b the distance from the back contact to the topgate, z distance from the back contact in the direction of growth and the electron charge e, e taken to be positive. The potential energy of the QD is determined by the lever arm a/b:

$$\phi(a) = -e\underbrace{\frac{a}{b}}_{1/\lambda}V_g. \tag{6.2}$$

Where a is given as the length of the tunnel barrier [49, 50]. It follows that the gate voltage allows for an adjustement of the QD-states relative to the Fermi-energy. If the QD-states are below the Fermi-energy, electrons can tunnel from the back contact into the dots. If the states are lifted above the Fermi-energy the electrons tunnel from the occupied states into the back contact. This kind of structures can thus be used to control the charging states of the QD and to tune their energy spectrum.
The bending of the electronic bands of the QDs influences the energy transitions in the QD and is called Quantum-confined Stark effect: The energy change of excitons trapped in QDs induced by an external field can be accurately described by a quadratic function of V_g, that takes into account the interaction of the electrical field with a permanent dipole p and the change of the bandedge, that leads to an additional separation of the electron hole wavefunction and thus to an induced polarizability β. The increased distance between the electron - hole decreases their attraction and blue shifts the excitonic energy. Furthermore the modified confinement potential lowers the energy states of the QD. The overall change is dominated by the red shift of the lowered eigenenergy states [22, 28]. The energy of an exciton E in an external electric field is given by [51]

$$E = E_0 - pF + \beta F^2, \tag{6.3}$$

where E_0 is the energy of the unperturbated exciton and $F = -(V_g - V_\mathrm{s})/b$

the electrical field strength between the Schottky-contact and the doped back contact.

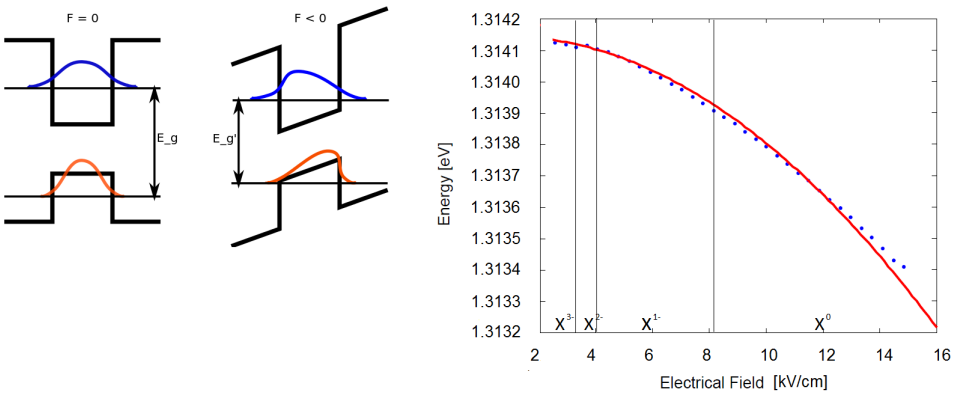

Figure 6.2: a) The variation of the excitonic transition energy as a function of an electrical field is shown. Due to the application of an electrical field the band edges are skewed. The electron and holes are repulsed/attracted in the direction of the minima of the potential. Resulting in a lowering of the energy and an reduced overlap. b) The quantum confined Stark effect as seen in the sample ES1795. The energy jumps due to charging are substracted and the data is fit with equation 6.3. The fit yields the values $E_0 = 1.3142$ eV, $p = 2.41e-02$ [cmV$^{-1}\mu$eV] and $\beta = 2.36e-07$ [cm^{2}V$^{-2}\mu$eV].

6.2 Micropillar cavity sample

This sample consists of QD embedded in micropillars cavities fabricated by "Laboratoire de photonique et de nanostructures" in Marcoussis, France. The distributed Bragg reflector micropillar cavities have been grown by MBE. The cavity is formed by two Bragg mirrors, which consists of thin layers of dieelectrics with alternating low and high refractive index (GaAs and AlAs). The highest reflectivity of a Bragg mirror is achieved when the layer thickness is equal to 1/4 of the optical wavelength. In this case, all reflections add in phase and the transmitivity of the mirror decreases exponentially as a function of the mirror thickness. Between these two mirrors is the active region with one optical wavelength, $\lambda = 976.1$ nm, thickness (called $\lambda-$cavity), embedding the InAs/GaAs QD in its center. The geometry confines the cavity in all three dimensions: In the vertical direction only one standing wave with the length of the cavity can be formed restricted due to the DBR and the lateral confinement, diameter = 3 μm. Due to the great

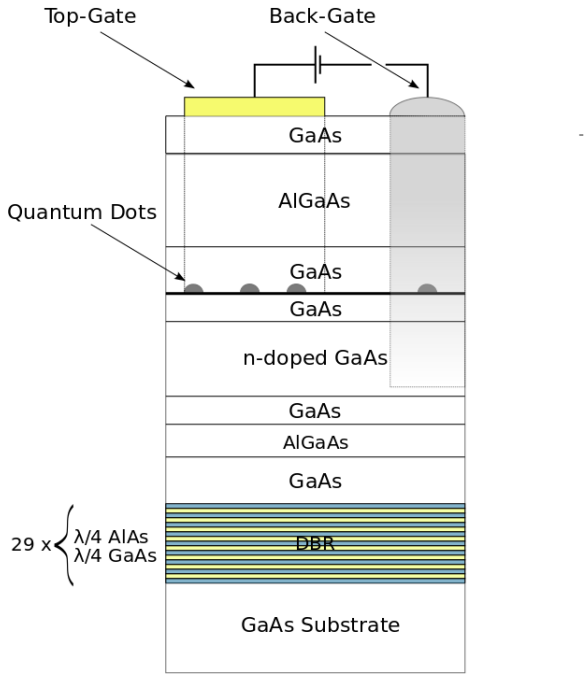

Figure 6.3: Layerstructure of ES1795.

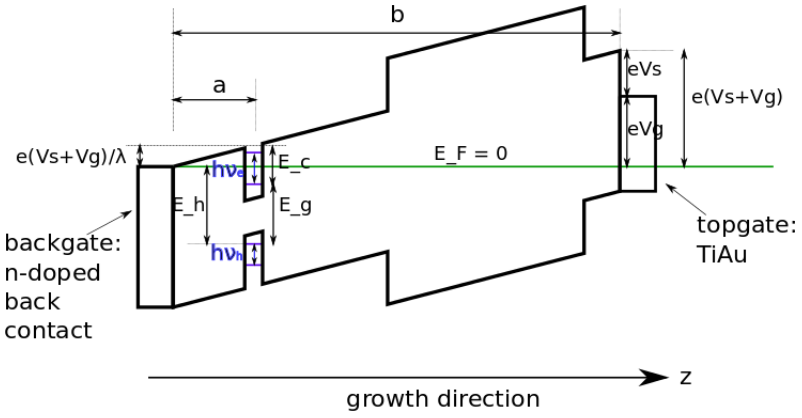

Figure 6.4: The corresponding schematic bandstructure of the field-effect structure.

difference between the refractive indices of GaAs (3.46) and air (1) [52], the allowed optical modes, the fundamental mode and higher order modes, are given by the solution of the Maxwell equations with appropriate boundary conditions [53].
An overview over the different micropillars are shown in figure 6.6 and the PL signal of micropillar QD26 is highlighted. The quality factor $Q = \lambda_c/\Delta\lambda$ of the cavity can be deduced from the μPL spectrum to:
972.15 nm/0.078 nm = 12000[4] It turned out that the different modes are sensitive to the spatial location and the size of the focal spot [55]. To maximize the fundamental mode the focus and position of the micropillar is adjusted. The measurement was carried out with the freespace collection path.

In order to bring the QD emission into resonance with the fundamental mode of the pillar, the energies of both must be tuned through each other. So far, there are two different tuning methods applied [56]: temperature tuning and electro-optical tuning. The electro-optical tuning of the excitonic states is based on the confined stark shift discussed in 6.3. This approach allows for a fast tuning of the emission without affecting the cavity mode, but requires additional preparations of the sample [57]. The second approach uses the different temperature sensitivity of the refractive index n (cavity) and bandgap (InAs QD). As seen in 6.5 the change of the CM (cavity mode) with increasing temperature in the measured range is approximatively linear, -0.01 meV/K at 40 K, compared to -0.07 meV/K at 40 K for the QD. The temperature dependency of the QD emission can be described with the simple Bose-Einstein type model [58, 59]:

$$E_{res}(T) = E_{res}(T=0) - S\hbar\omega\left(\coth\frac{\hbar\omega}{2k_BT} - 1\right). \tag{6.4}$$

Here S is a dimensionless coupling constant and the coth term describes the electron-phonon coupling to phonons of the energy $\hbar\omega$, according to the Bose-Einstein occupation number of the phonon mode. This model is normally applied to model the energy shift of the bandgap of bulk semiconductors, indicating that unlike for nanocrystals the $E(T)$ dependence

[4]The true content of this value has to be questioned. From [54] it is known that the Q-value drastically depends on the excitation power and saturates at high pumping power to its correct value.

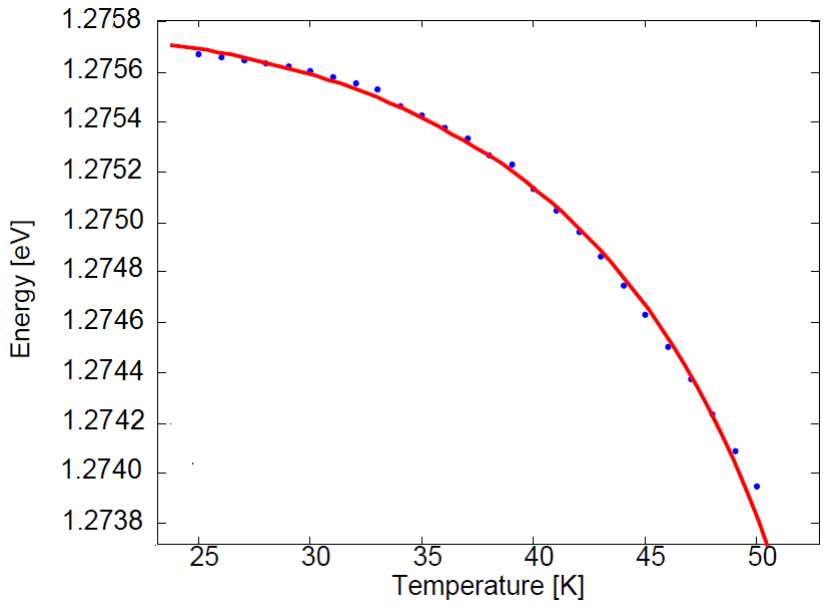

Figure 6.5: Energy of the QD as a function of the temperature. The red line is the fit. The fit predicts the energy behavior very well in the range 25 K up to 45 K, but overestimates the shift for higher temperatures.

in self assembled InAs QD are dictated by the same mechanisms as for bulk. The best fit is obtained for $S = 0.065$ and $\hbar\omega = 11$ meV.

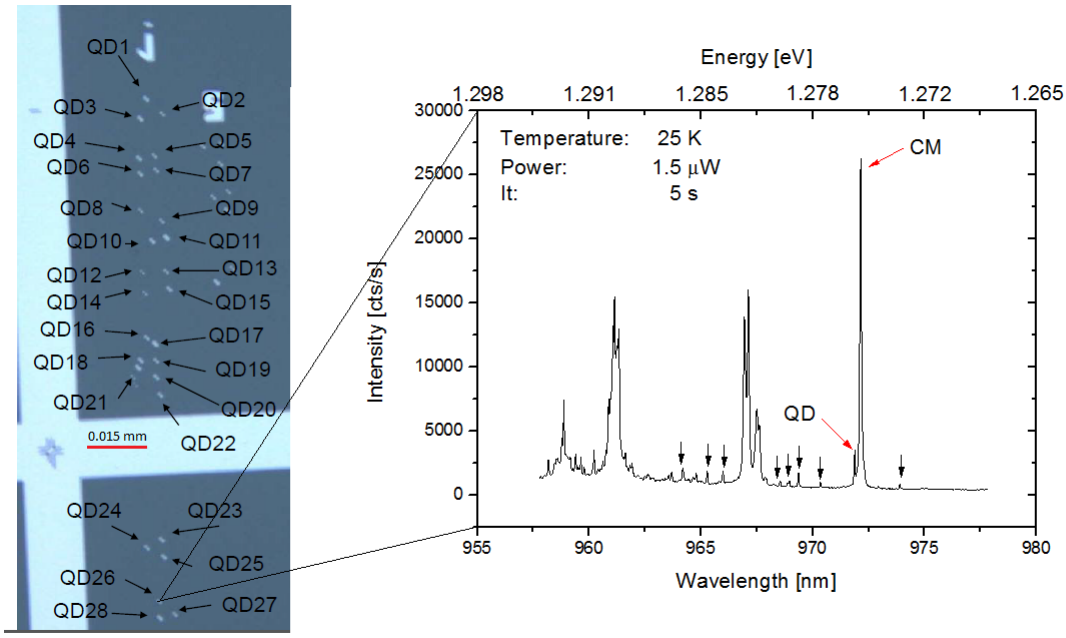

Figure 6.6: The PL measurement was done in freespace. The left image shows a 10x magnified microscope image of the single micropillars (QD1 to QD36). QD26 is intersting because it not only shows high counting rates for the fundamental cavity mode and excitons but also their energies are spectrally close to each other. The fundamental cavity mode and nearest exciton is indicated by a red arrow. The black arrows marks other exciton lines.

Chapter 7

Measurements

The main goal of these experiments was to provide evidence that it is possible to carry out resonance fluorescence measurements with the optical setup as introduced in chapter 5.
The sample that we used for the resonant excitation of QDs was a field-effect structure, ES1795, with a Bragg mirror below the QD layer to enhance the signal. The first step in testing the system on its resonance fluorescence capabilities is the localisation of a bright single QD. The second step is the characterization of the QD. We perform gate sweep measurements at 9.3 K on the QD to identify its states, their resonance frequencies and the extent of the Stark shift, discussed in section 7.1.1. For the resonance experiments (section 7.2) the X^- state is chosen and tuned by the applied laser. A strong enhancement of the photon emission at the crossing of QD and laser has been detected. To verify if the electronic transition of the QD is resonantly driven, a power dependent measurement is performed, where the well-known power broadening of the exciton linewidth and power saturation is observed. The other measurement concerns the coupling efficiencies of the microcavities to the SMF. The photon collection efficiency depends on the design and size of the individual micropillars. The coupling efficiency is measured by means of resonance fluorescence and time resolved PL, where the resonantly scattered photons of the QD in resonance with the fundamental cavity mode are counted by CCD2. The time resolved PL measurement gives us the decay time for the excitons in the cavity and determines the theoretically possible number of detectable photons. Here, we demonstrate the possibility of a measurement of the coupling efficiency. For that, the crossing of the QD emission with the cavity mode has to be detectable for the fiber based

detection path. For that purpose the fiber and freespace detection paths are compared.

7.1 Field-effect sample

7.1.1 Non-resonant measurement: Decoding single QD spectra

The first step to carry out resonance fluorescence measurement was to find a bright single QD. The brightest QD found is shown in figure 7.5. The single spectrum does not allow identifying the spectral lines, furthermore no DC stark shift can be extracted which is needed to convert the applied voltage in energy, see below. To get these information a gatesweep is performed.
As discussed in chapter 3 different excitonic complexes can exist in QDs and due to different Coulomb interactions between the charge carriers their emission differs in energy. The distinct transition frequencies of the different occupancy states can be used to assign an exciton complex to a spectral line, considering the fact that the only "constant" value is the 6 meV difference in energy between neutral exciton and negative trion, where the negative trion is always on the low energy side of the neutral exciton as seen in section 3.3. It follows that the negative trion and neutral exciton can be identified with much effort. For the other spectral lines aditional measurements have to be carried out to distinguish between the states such as the power dependency of their emission. In the following the decoding process is discussed.

Charging Quantum Dots means the study of the behaviour of the QD under the influence of an electric field. As mentioned in section 6.1, the application of an electric field gives rise to a bending of the band edge and with it a control mechanism to load electrons into the QD when the Fermi energy crosses the energy states of the QD. If an electron is located in the QD, the state is prohibited for another electron to tunnel into the QD as long as the energy gain for an tunnel process is less than the cost of the Coulomb blockade. This effect leads to a non-continuous change between the different excitonic states [60]. As a result the different charge states appear at distinct voltage ranges, which can be used to control the number of electrons in the QD. Although the QD are deterministically charged at a certain time the different states overlap (figure 7.4). This can be explained by taking into account that every spectrum is integrated over several seconds. Furthermore

the barrier thickness and the non-resonant excitation plays a crucial role. The thicker the tunnelbarrier, the lower is the tunneling rate, and it needs more time to get into "equilibrium" with the electron reservoir of the back gate. If this process is slower than the recombination of the electron-hole pairs, the lines overlap [36].

The color map (figure 7.4) presents the discrete PL signature of a single QD as a function of an applied vertical field. This graph consists of a series of single spectra recorded for 5 s and differing by a voltage of 0.02 V. The colors indicate the number of detected events, red and blue mean high and low intensities (dark blue is the background). The x and y axis stand for the gate voltage along the growth direction and the PL wavelength of the QD, rescpectively.

For $|F| > 15$ kV/cm ($V_g < -0.2$ V), no PL lines can be observed. This can be explained by considering the n-type Schottky diode structure (6.4). The QD energy states are higher than the Fermi-level (no tunneling from the backgate to the QD), consequently, the only electrons trapped in the QD come from the optical excitation. Furthermore, the stronger the applied field, the more transparent the barrier gets, leading to a shortened tunneling time. A photon generated electron-hole pair relaxing into a QD cannot optically recombine, if the tunneling time is less than the radiative lifetime of the neutral exciton. The much lighter electron ($m^*_{\mathrm{e:GaAs}} = 0.066 \cdot m_e$, $m^*_{\mathrm{hh:InAs}} = 0.4 \cdot m_e$) tunnels into the backcontact, leaving a hole filled QD behind that can form a positive trion (X^+) with another electron hole pair. Therefore, PL lines at large negative bias are expected to be positive trion states. The neutral exciton should appear when the tunneling time is reduced to its radiative lifetime. Charging of the QD with an additional electron from the backgate are expected to happen at lower electrical fields due to the energy needed to get the QD energy eigenstates in resonance with the the Fermi level and to overcome the interaction energies (Coulomb blockade).

The first PL signal is observable if the recombination time equals the tunneling time. This happens at -0.16 V. The appearing PL line is indicated to come from the positive trion (X^+). The measured PL intensity increases monotonically and saturates at -0.04 V, compare with figure 7.1. A consequence of the continously reduced tunneling probability of the electron to the back contact for an increasing gate voltage, the electron remains in the QD. The next PL lines emerge at 0.00 V and are assigned to the neutral exciton (X^0)

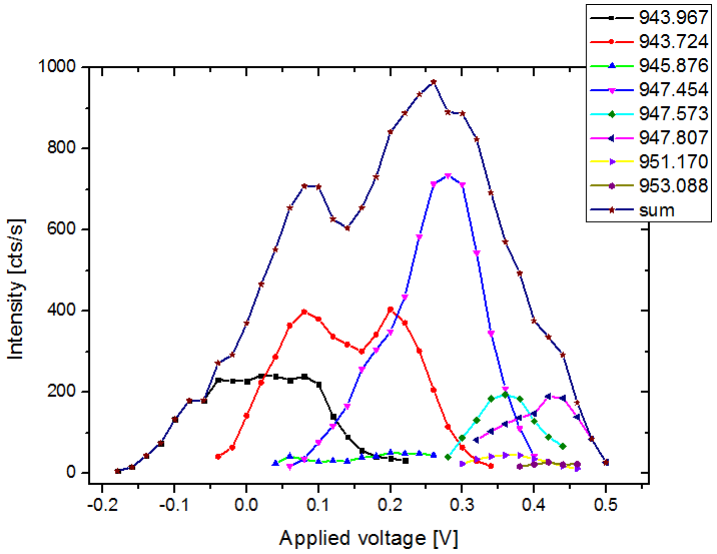

Figure 7.1: The integrated PL intensity of the different excitonic states as a function of the bias is shown, the lines are guide to the eye. In the range of -0.2 to 0.5 V, different excitons exists.

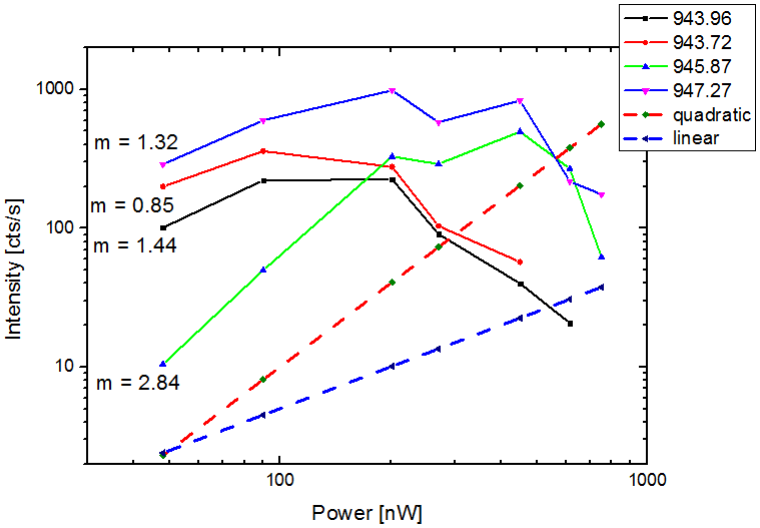

Figure 7.2: The black (X^0), red (X^+) and blue (X^-) solid lines show an approximative linear dependency on the excitation power in contrast to the super quadratic dependency of the biexciton (green solid line). The slope of every curve is indicating at their start (labeled m) and determined on the low excitation dependency (48 - 90 nW). The unusual super linear and super quadratic behavior is mainly due to the small amount of data points.

and the neutral biexciton (XX^0). The biexciton state appears at higher excitation powers and was not seen in the lower power gatesweep (48 nW), which is a strong indication of its biexcitonic nature. The power dependency measurement revealed for this line a quadratic increase with the pumping power, as expected for a biexciton (shown in the graph 7.2 and 7.3). The energy seperation between the trion and neutral exciton signal is about -0.13 meV, with a lower energetic trion state. Which is in contrast to the simple model introduced in section 3.3. As discussed with Dr. Martin Kroner and mentioned in 3.3 the positive trion state is usually less tightly bound than the neutral exciton, in agreement with the relative strengths of the Coulomb interaction terms 3.15. However, every QD is different and exhibits different binding energies for X^+ and XX^0. They can be either red or blue shifted with respect to the neutral exciton. Surprising is the fact that for every InAs/GaAs QD the negative trion state is always around 6 meV on the red side of X^0.

The negative trion state appears at +0.06 V and is measured to be 5.4 meV on the low energy side of the X^0. From this can be deduced that $|C_{eh}| > |C_{ee}|$ [1] , resulting in a stronger bounded state.

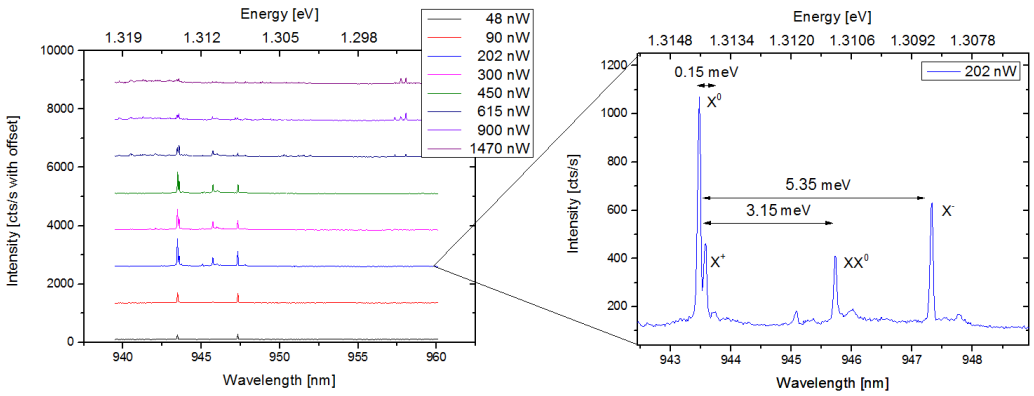

Figure 7.3: Left: The spectra have been taken at 0.2 V from figure 7.4 for different pumping powers. At low excitation power (48 nW) only two peaks are visible coming from the neutral and negatively charged exciton, at higher power the biexciton shows up. Right: The enlargement of the 202 nW spectrum with the respective excitonic states and their energy differences.

Because the s-shell in the QD is filled with two electrons of opposite spin (Hunds-rule), the next charging of an electron is expected to happen at

[1] $E_{PL}(X^-) - E_{PL}(X) = -C_{eh} + C_{ee}$

much higher gate voltages due to the beginning of the filling of the p-shell. The next exitonic complexes X^{2-} and X^{3-} appear at 0.28 V and 0.32 V. The characteristics of these states is their splittings into two possible final states differing by their spin wavefunctions: singlet (low energy), triplet (high energy) for the X^{2-} and doublet (low energy), quadruplet (high energy) for the X^{3-} [61]. Because these states are low in intensity and their linewidth is comparably broad they are unattractive for the resonant excitation and are thus not further considered in this work.

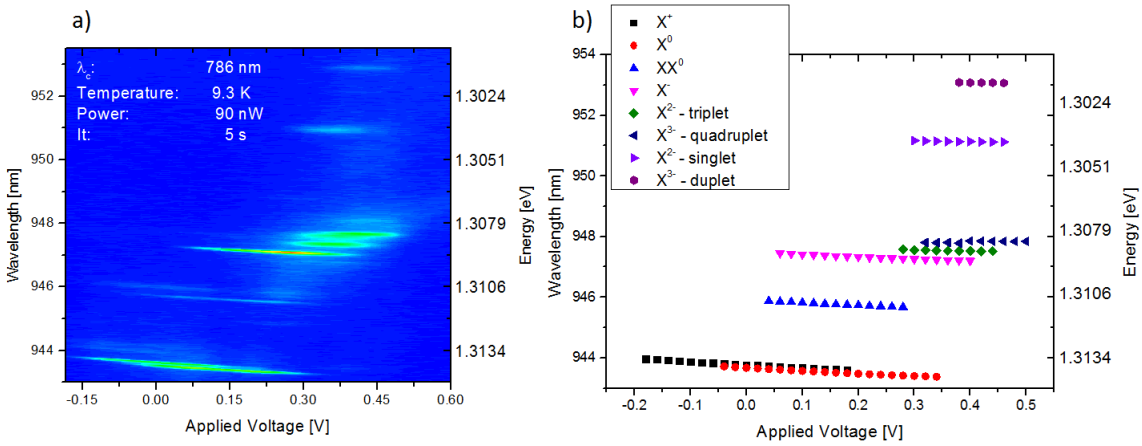

Figure 7.4: Photoluminescence signal of a single QD as a function of voltage. In the range between -0.2 V and 0.3 V several different energy states are visible. At more negative gate bias this region no excitons exist because they are ionised by the strength of the applied field. The different plateaus can be readily identified with the corresponding excitonic state.

7.2 Resonant measurement of X^- state

The gatesweep discussed in the previous section is used as a basis for the resonant fluorescence measurement. We focus on the brightest excitonic state of the QD, X^-, with its peak location at 947.27 nm (figure 7.5).

Unlike the neutral exciton X^0, which has a fine structure splitting, the X^- state manifests itself in a single Lorentzian line at zero magnetic field [28]. Additionally, we can learn from the above applied gate sweep how strong the Stark shift is. This is later used as a conversion factor from gate bias the photon energy.

The normal approach is to scan the laser over resonance of the quantum

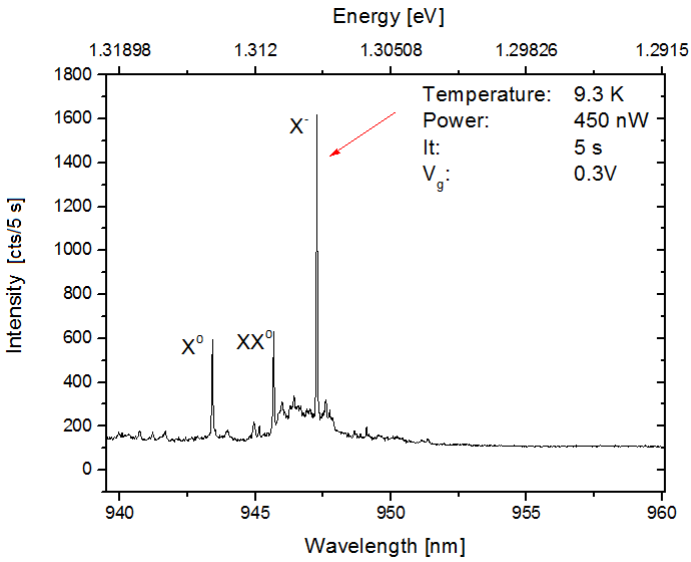

Figure 7.5: The red arrow marks the focused excitonic state. The applied voltage of 0.3 V corresponds to the highest possible signal intensity.

emitter. However, the cavity tuning of the laser itself influences the suppression of the laser in the detection path [2], and leads to fluctuations in the detected signal. To circumvent the suppression problem occuring during tuning of the laser, the QD is tuned instead.

By the first successfully accomplished resonant scan of a QD, the laser is tuned to the resonance wavelength of 947.27 nm. The crossing between QD and laser can be clearly seen in figure 7.7, where at an emission wavelength of 947.25 nm no crossing can be observed (7.6). The suppression of the laser was $1 \cdot 10^6$ [3], and it appears that a suppression of about 1 million is needed to see the resonant photons of the QD. With a suppression of $0.4 \cdot 10^6$, no resonant signal was detected. Except for the good suppression, an exceptionally high coupling efficiency of 78% was achieved.
To show the true nature of the resonant fluorescence signal, the quantum emitter was resonantly probed at various excitation powers from 51 nW up

[2] tuning the emission wavelength by 60 pm (voltage difference of 3 V) reduces the suppression by a factor of 1.5 to 2.

[3] The suppression factor is measured with a voltage amplifier, section A and a voltmeter. The suppression is the relation between the signal strength, given as the height of the gain and voltage, of the backreflected laser with POL1 in the path and neither $\lambda/4$ nor POL2 and POL1 and POL2 inserted in the path.

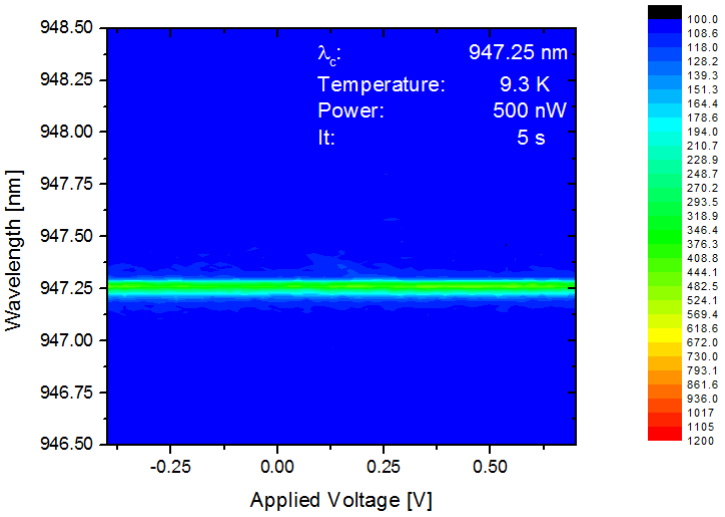

Figure 7.6: The QD was tuned from -0.4 to +0.7 V where the laser is suppressed by a factor of $1 \cdot 10^6$. The laser is to far off-resonant to excite the QD. The constant counting rate shows the stability of the system and suppression.

to 10 μW measured in front of the MO (compare figure 5.1) to see if it shows the well-known power saturation behavior of a two-level system, as discussed in 4.1.
The obtained resonance fluorescence gate voltage scans 7.7 are then summed up in the region 947.27 ± 0.035 nm to get the complete signal at resonance and at the same time to increase the signal to noise ratio.

In order to study the power dependences of the various scans, they are fitted with Lorentzian profiles to determine their heights [4] and the linewidths (FWHM). To get the linewidths in units of wavelength (energy), the obtained linewidths from the measurement are converted with the conversion factor obtained from the linear stark shift: 0.75 nm/V. The results for the 51 nW and 1510 nW scans are shown in figure 7.8. The obtained data of the Lorentzian curve fits, height and linewidth, are then simultaneously fitted in dependence on the applied power in Matlab with the model functions 4.22 and 4.23, respectively.
To take into account charge fluctuations in the environment of the QD, resulting in spectral fluctuations of the excitons, a constant factor c = 1.3 μeV, as in reference [28], is added in order to fit the FWHM curve.

[4] height = (height at resonance of Lorentzian curves) - (average height of the background)

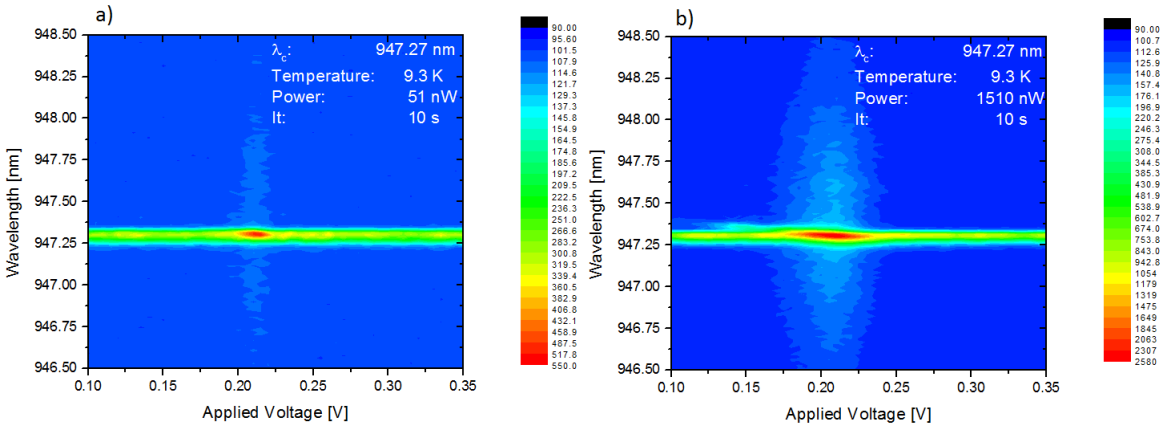

Figure 7.7: Spectrally (ordinates) and voltage (abscissas) resolved fluorescence image for a resonantly driven QD. The laser line appears as a greenish line and the red peak at 0.21 V marks the crossing of QD and laser. The convolution of the QD signal with the signal of the laser leads to the broadening at the crossing point. a) The detuning region is much narrower compared to b), a direct consequence of the power broadening discussed in section 4.1

From the fits the obtained values are $\gamma = 6.2$ μeV and $P_{\text{sat}} = 530$ nW, corresponding to a linewidth of 12.4 μeV. The linewidth is assumed to be affected by the real temperature felt by the QDs. As mentioned in section 5.5.2, the temperature shown by the temperature controller does not have to be the true value of the sample. It is known that InAs/GaAs QDs can show line broadening effects for temperatures above 10 K [58]. In this reference several QDs are measured and they show various temperature dependences. The "temperature sensitive" QD has a linewidth of 4 μeV at 5 K and 12 μeV at 17 K, indicating that the temperature could be several K higher than the measured values of the cold finger.

From parameter $b = \eta \cdot \gamma_{\text{spon}} = 730$ the collection efficiency of the optical setup can be estimated. By assuming $\gamma_{\text{spon}} = \gamma$ [5], the resulting collection efficiency is $\eta = 5 \cdot 10^{-7}$. This value corresponds to the lower limit of the collection efficiency and deviates by a factor of 60 from the calculated value, $3 \cdot 10^{-5}$, in section 4.1. This deviation can be explained by the assumption made to calculate the collection efficiency, $\gamma_{\text{spon}} = \gamma$ and by taking into account the TiAu Shottky gate, which was not considered in the former calculations.

[5] γ is the upper bound of γ_{spon}

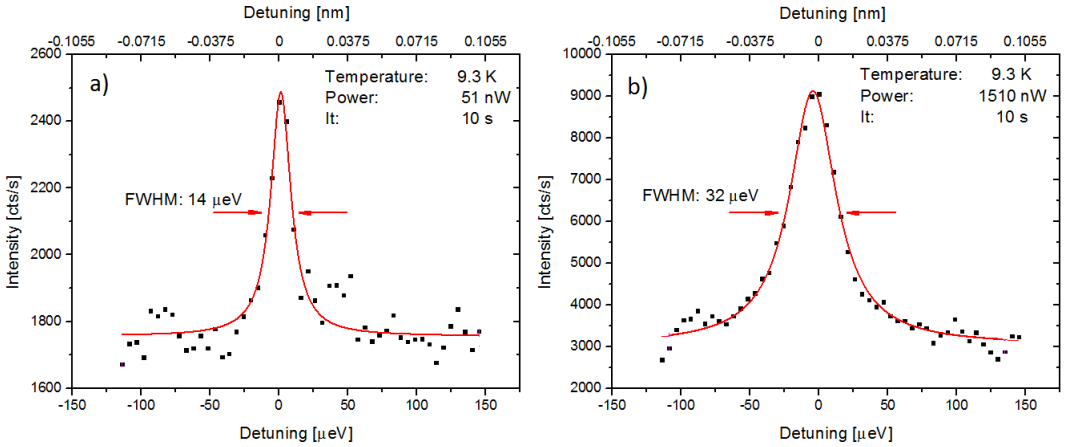

Figure 7.8: Shown is the integrated signal in the wavelength range around the peaks. a) the peak reveals a linewidth of 14 μeV which is broader than the calculated linewidth at zero pumping power, 12.4 μeV, showing that the laser power causes already a broadening. b) the peak is more than 2 times braoder than the initial value.

It is expected that it reflects 30% of the incident photons. A minor but non-negligible role plays the effective transmission of the spectrometer, which is likely to be lower than assumed for η_{spec} (see section 4.1)

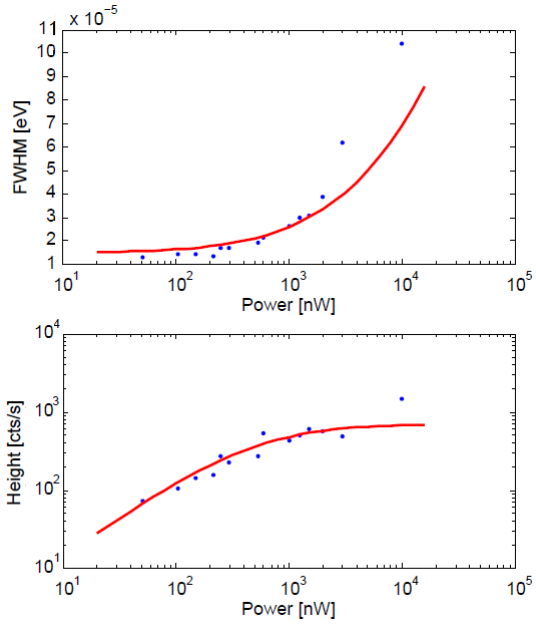

Figure 7.9: Power broadening and saturation of a single resonantly pumped QD. The low intensity limit of the linewidth is 12.4 μeV and the power saturation is 530 nW.

7.3 Micropillar sample

7.3.1 Detectability of the crossing between QD cavity modes for the fiber detection path

The coupling efficiency of the cavity modes is of central importance for cQED experiments and depends strongly on the geometry of the micropillar [62]. As mentioned in section 7.2, SMFs contribute significantly to the laser suppression in the crossed polarization technique. This technique is also used in the quantum entanglement experiments between a semiconductor quantum dot spin and the colour of a propagating optical photon in the quantum photonics group [63].
To see if microcavities can be characterized, the crossing between exciton emission and resonator modes are investigated.

For this we excite the QD located in the micropillar structure, QD5 (see figure 6.6), with the DL1 and the emission wavelength is changed by 1 K steps from 37 K up to 60 K. When the QD is in resonance with the fundamental cavity mode, the crossing is observed as a peak in the spectrum,

indicated by a red arrow in figure 7.10. The increase at resonance in the countrate is low, which is believed to come from the low excitation power of 100 nW [64] and the low quality factor of the micropillar. The left side of figure 7.10 shows the power spectrum in the vicinity of the crossing. An obvious difference between fiber and freespace detection is the enhancement for the on and off resonant countrate. For the fiber detection the counts increase by a factor of 1.6 in comparison to 1.2 for freespace. In the freespace detection no restrictions exist for the propagating modes leading to a reduced increase of the intensity between off and on resonance, in contrast to the fiber where only Gaussian modes are supported. As long as the QD interacts with the continuum of non-resonant modes it will emit the photons in an undirected way and it cannot be coupled into the SMF. However, in the case of good spectral agreement of the QD emission and the cavity mode the photons are channeled in the cavity mode and can be coupled into the SMF.

Although the signal intensity at the crossing is weak, it could be shown to detect the increase in the signal intensity at resonance, which allows for characterization of microcavities e.g. determination of Purcell factor and coupling efficiencies discussed above.

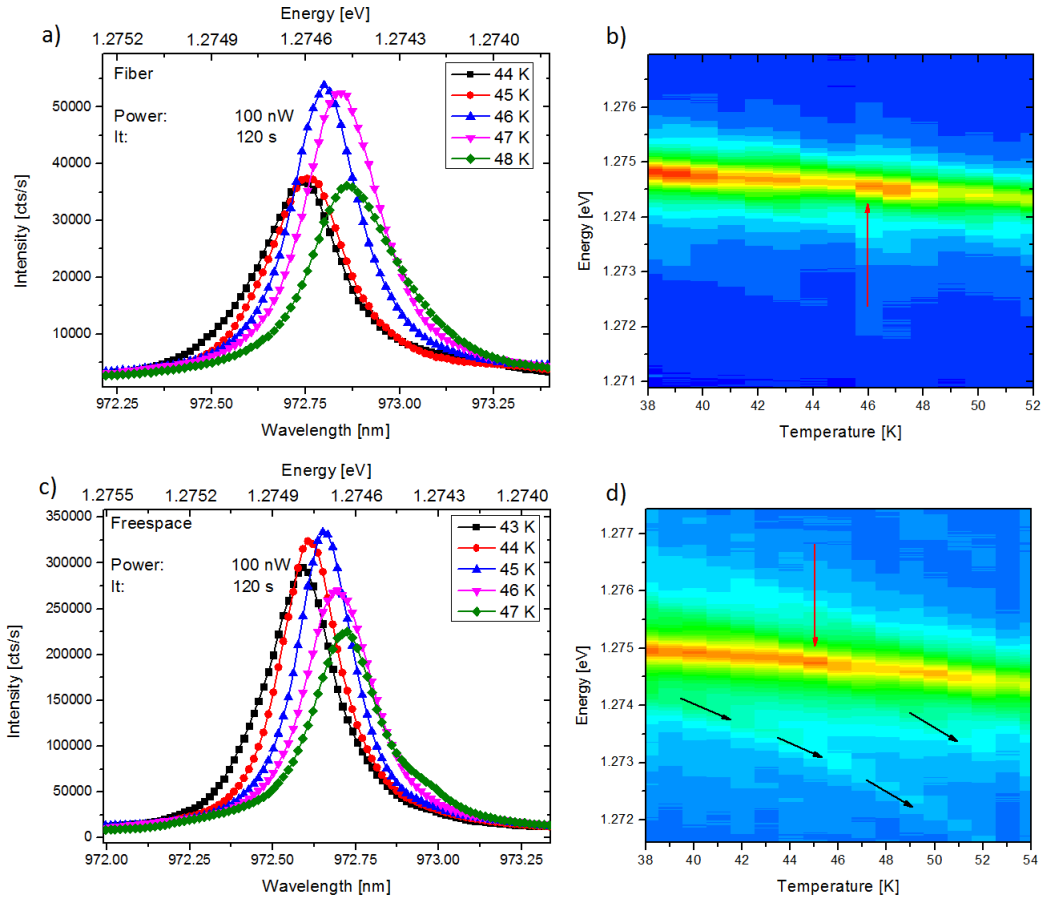

Figure 7.10: a) and b) show the crossing of the QD and CM for the fiber detection path and c) and d) for the freespace detection path. Obvious is the difference in suppression of the non-resonant modes in b) and c). The red arrows indicate the crossing of QD and CM investigated in a) and c) and the black arrow shows the exciton emission, only visible in the freespace detection.

Chapter 8

Conclusion and Outlook

In conclusion, we have demonstrated the possibility to use a fast characterization optical setup for resonance fluorescence measurements on single QDs. Resonance fluorescence measurements open up the possibility to measure the true linewidth of single QDs, which is an important criterion of the quality of the sample. This was done for a suppression of the laser of $1.0 \cdot 10^6$ and tuning the QD into resonance with the applied laser.

The next logical step would be to tune the laser into resonance with the QD. This is best done by mechanically tuning the laser into resonance with the QD and thus only a minor change in the emission wavelength of the laser is needed such that the suppression should remain stable. With this experiment a higher flexibility of the setup could be demonstrated, which is of great importance for resonance fluorescence measurements of non-gated samples. Furthermore, a standardized and fast way to carry out resonance fluorescence measurements has to be found, such that resonant experiments on QDs can be done within one day.

Although the measured suppression of over $1 \cdot 10^6$ is satisfying, the obtained signal to noise ratio of 2 - 6 is low in comparison to other resonant scattering experiments [65, 66]. Furthermore, high suppression factors are not trivial and time consuming to obtain. It is thus of great importance to find a reliable way to get high suppression factors or to increase the signal intensity.

We anticipate that the low signal to noise ratio could be the consequence of a non optimized coupling into the SMF. This can be verified by optimizing the coupling efficiency of the resonantly scattered photons when the QD is in resonance with the laser.

Furthermore, the characterization of microcavities could be demonstrated. The next step is to install a pulsed laser which in combination with resonance fluorescence enables to measure the coupling efficiencies of micropillars, as discussed in the introductory text of chapter 7.

Appendix A

Alignment

This section is only intended for users of this optical setup, as the alignment process will be discussed. Some characteristic numbers (coupling efficiencies) are given to ensure a comparable alignment. The alignment was done in advance for every single measurement and recorded to be able to compare the results obtained during a measurement.

As soon as the whole system has reached the equilibrium temperature at 9.3 K the alignment of the optical setup can be made[1].

For the alignment the laser DL2 is used because it emits at a comparable wavelength as the investigated QD. First the coupling of the alignment laser is checked. It should be over 5 V at a gain of 10^5 [2], which can be done by connecting SMF1 to the sensor of the current to voltage amplifier from FEMTO. This ensures that not only enough power goes into the fiber but also the strongest mode is coupled. Otherwise it is a sign that the coupling is not optimal or the diode laser is broken[3]. The next step in the alignment is the coupling into the MO. If the laser is coupled into the MO an airy pattern is imaged on the CCD1. To check the quality of the coupling it is recommended to drive through the focus and see if the spot remains at the same position and no change (ellipsoidal) in the pattern is visible. Also the pattern should show homogenously illuminated rings, best seen if the laser is out of focus. In most cases a misaligned beam can be corrected with the

[1] The time needed for our cryostat at 300 K under vacuum 10^{-5} mbar down to 9.3 K is around 45 to 60 min.

[2] For DL1 similar values are obtained: gain 10^5 and usually over 2 V.

[3] This can happen if the power supply is not switched off during a change between DL1 and DL2.

usage of M8.
Afterwards the pattern is refocused and the central intensity circle is marked on the screen. This marking is made to see if the excitation path (defined by SMF1 and SMF2) is overlapping with the detection path to ensure that the excited area is equivalent to the detected area. This is done by connecting SMF1 with SMF3. The pattern looks slightly different because the airy pattern from the MO overlaps with the reflection from the PBS. Most important is that the center of the detection path is identical with the marking. Otherwise this can be corrected by walking the beam with M9 and M10 towards the cross. When both spots overlap (excitation spot and detection spot) and their spot resembles an airy pattern the system is already quite well aligned.

Next, the light coming from the MO is collimated. This is done by installing a mirror between POL2 and PBS to decouple the backreflection from the sample surface. The mirror is best adjusted in such a way that the beam path for the decoupled light is widest. It is made visible by the use of an infrared card (IR card). The focus is then set to infinity (spot diameter remains the same along the optical path). Afterwards the mirror is removed. The MO is now in focus for the emission wavelength of the QD. In the last steps of the alignment procedure the fine adjustment and the coupling into the spectrometer is accomplished. To achieve this SMF3 is connected with the FEMTO and the coupling efficiency $\left[= \frac{\text{at outpuf of SMF3}}{\text{at input of SMF3}}\right]$ is maximized with M9 and M10. The coupling efficiency is then checked with the power meter (PM). The coupling efficiency should be at least $30 - 45\%$ [4], good values are 50%+ and the best value measured so far was 78%. The theoretical coupling efficiency assuming that we do not have any mechanical misalignments, no manufacturing tolerances of the fiber and a perfectly gaussian mode, would be 98% [5] The last step is the coupling into the spectrometer. The normal process is to check first with WinSpec[6] in the image mode and $m = 0$ order (grating adjustment $\lambda_c = 0$ nm) how many pixels are covered by the alignment laser. Optimally, there would be a single bright pixel. Usually it was one bright pixel sourrounded by four dimmed pixels and centered on the

[4] normally between 35 - 45 %

[5] the coupling efficiency can be calculated with [67]: $\frac{r_{fiber}^2 \omega_{FWHM}^2}{\left(r_{fiber}^2 + \omega_{FWHM}^2\right)^2}$, the radius of the fiber is 2.3 μm and the beam waist is determined by using 5.2, the NA of CM3, 0.15, $\lambda = 980$ nm and T = 1.2: $\omega_{FWHM} = 2$

[6] Princeton Instruments Software package for communicating with the spectrometer.

CCD2 (WinSpec: $X = Y = 0$) to avoid abberations [47]. The adjustment of the beam on the CCD is achieved by moving the U-bench in the x-y-z directions. When the spot is satisfyingly alligned the ROI (region of interest) is set: $X = 1340, Y = 25$ pixels around the spot. The limitation of $Y = 25$ instead of the full height of the CCD2 is for the reduction of the noise (dark current, scattered light) and $X = 1340$ means that the full spectral range of the grating/CCD2 is available (compare section 5.5.3) and switch WinSpec to the spectra mode, $m = 1$ (grating adjustment $\lambda_c = 980$ nm). Now the fine tuning has to be done by using once more the xyz-stage for the U-bench. The goal is to maximize the peak intensity and at the same time to get the narrowest FWHM (activate the focus helper). After this, the slit has to be closed until the intensity starts to decrease.

The alignment of the freespace detection path is very similar to the fiber-based detection path. Only the differences are mentioned here: The coarse alignment of the optics is done with the HeNe. Next to M13 is an aperture, not shown in figure 5.1, parallel to the spectrometer entrance, and the height of the center coincides with entrance slit center. The coupling lens, L4, is removed. The beam is adjusted by controlling M12 and M13 to go through the center of the aperture and onto the center of CCD2, which runs in the image mode. The laser is changed to the alignment laser. L4 is then set into the beam path so that there is no deviation from the original adjustment. The fine tuning can be done by the translation mount of L4 in x-y (lateral position) and the micrometer table, mounted on in z direction (focus). The remaining procedure is the same.

After this the whole setup is ready to carry out the experiments.

Appendix B

Collection Efficiency Parameter C_{geom}

The collection efficiency of the MO can be estimated by modeling the QD as a dipole emitter in a medium with refractive index $n = 3.46$ and the dipole moment with an angle δ_{em} with respect to the symmetry axis of the collection optics. The emission power of a dipole emitter is given as

$$dP = \frac{3}{8\pi} \sin(\theta')^2 \theta' d\Omega'.$$

The collection efficiency C_{geom} is obtained by the integration of B over the solid angle bounded by θ_{max} [30]

$$C_{\mathrm{geom}} = \frac{1}{8}\left[4 - 3\cos(\theta_{max}) - \cos(\theta_{max})^3 + 3\left[\cos(\theta_{max})^3 - \cos(\theta_{max})\right]\cos(\delta_{\mathrm{em}})\right],$$

where θ_{max} corresponds to the angle which is covered by the MO,

$$\theta_{max} = \arcsin(\mathrm{NA}/n) = \arcsin(0.55/3.46) = 0.15.$$

It follows for dipole moments lying in the plane of the sample ($\delta_{\mathrm{em}} = \pi/2$), that

$$C_{\mathrm{geom}} = 0.008.$$

Bibliography

[1] A. Zrenner, "A close look on single quantum dots," *Journal of Chemical Physics*, vol. 112, p. 7790, 2000.

[2] R. Warburton, "Single spins in self-assembled quantum dots," *Nature materials*, vol. 12, p. 483, 2013.

[3] P. Michler, *Single Semiconductor Quantum Dots*. Springer, 2009.

[4] A. Heogele et al., "Fiber-based confocal microscope for cryogenic spectroscopy," *Review of Scientific Instruments*, vol. 79, no. 023709, 2008.

[5] M. Koskinen et al., "Hund's Rules and Spin Density Waves in Quantum Dots," *Phyiscal Review Letters*, vol. 79, p. 1389, 1997.

[6] L. Kouwenhoven and C. Marcus, "Quantum Dots," *Physics World*, vol. 11, p. 35, 1998.

[7] V. Tuerck, *Elektronische Eigenschaften einzelner Halbleiterstrukturen*. PhD thesis, Faculty II - Mathematics and Science Technical University Berlin.

[8] S. Kako et al., "A gallium nitride single-photon source operating at 200 K," *Nature Materials*, vol. 5, p. 887, 2006.

[9] P. Maletinsky et al., "Dynamics of Quantum Dot Nuclear Spin Polarization Controlled by a Single Electron," *Physical Review Letters*, vol. 99, no. 056804, 2007.

[10] C. Latta et al., "Quantum quench of Kondo correlations in optical absorption," *Nature*, vol. 474, p. 627, 2011.

[11] A. Reinhard, *Strong Photon-Photon Interaction in Solid State Cavity QED*. PhD thesis, Institute For Quantum Electronics at Swiss Federal Institute Of Technology Zurich.

[12] S. Kim, "Performance of light-emitting-diode based on quantum dots," *Nanoscale*, vol. 5, p. 5205, 2013.

[13] S. Buckley, K. Rivoire and J. Vockovic, "Engineered quantum dot single-photon sources," *Rep. Prog. Phys.*, vol. 75, no. 126503, 2012.

[14] B. Joyce et al., *Quantum Dots: Fundamentals, Applications, and Frontiers*, vol. 190. Springer.

[15] V. Mlinar et al., "Structure of quantum dots as seen by excitonic spectroscopy versus structural characterization: Using theory to close the loop," *Physical Review B*, vol. 80, no. 165425, 2009.

[16] R. Seguin, *Electronic Fine Structure and Recombination Dynamics in Single InAs Quantum Dots*. PhD thesis, Faculty II - Mathematics and Science Technical University Berlin.

[17] B. Joyce, D. Vvedensky, "Self-organized growth on GaAs surfaces," *Reports: A Review Journal*, vol. 46, p. 127, 2004.

[18] I. Itskevich et al., "Stark shift in electroluminescence of individual InAs quantum dots," *Applied Physics Letters*, vol. 76, p. 3932, 2000.

[19] R. Warburton et al., "Optical emission from a charge-tunable quantum ring," *Physical Review B*, vol. 405, p. 926, 2000.

[20] M. Sigrist, "Solid State Theory." `http://www.itp.phys.ethz.ch/education/fs13/sst`. [Online; accessed August-2013].

[21] A. Zhou and W. Sheng, "Electron and hole effective masses in self-assembled quantum dots," *European Physical Review B*, vol. 68, p. 233, 2009.

[22] T. Warming, *Elektronische Struktur angeregter Zustände einzelner InAs-Quantenpunkte*. PhD thesis, Faculty II - Mathematics and Science Technical University Berlin.

[23] Wolfgang Stumpf, *Studies on Fundamental Technologies for Fabrication and Evaluation of Combined Photonic Crystal Nanocavity-Quantum Dot Devices*. PhD thesis, Kyoto University Japan.

[24] X. Wen-Fang, "Binding Energies of a Positively Charged Exciton in a Quantum Disc," *International Academic Publishers*, vol. 44, p. 925, 2005.

[25] I. Kupchak et al., "Excitons and trions in spherical semiconductor quantum dots," *Semiconductor Physics, Quantum Electronics & Optoelectronics*, vol. 9, p. 1, 2005.

[26] M. Bayer et al., "Hidden symmetries in the energy levels of excitonic "artificial atoms"," *Nature*, vol. 405, p. 923, 2000.

[27] P. Dalgarno, "Calculation and Construction of Scale Drawing for Exciton Moedelling (Red Dots)." 2003.

[28] M. Kroner, *Resonant photon-exciton interaction in semiconductor quantum dots*. PhD thesis, Faculty of Physics Ludwig-Maximilians-University Munich.

[29] G. Sek et al., "On the applicability of a few level rate equation model to the determination of exciton versus biexciton kinetics in quasi-zero-dimensional," *Journal of Applied Physics*, vol. 108, no. 033507, 2010.

[30] T. Plakhotnik et al., "Single molecule spectroscopy: maximum emission rate and saturation intensity," *Optics Communications*, vol. 114, p. 83, 1994.

[31] G. D. Gilliland, "Photoluminescence spectroscopy of crystalline semiconductors," *Elsevier: Materials Science and Engineering: R: Reports*, vol. 18, p. 99, 1996.

[32] D. Sreenivasan, *Capture, relaxation and recombination in quantum dots*. PhD thesis, Department of Applied Physics of the Eindhoven University of Technology.

[33] C. C. Tannoudji, *Atom-Phton Interactions: Basic Processes and Applications*. Wiley, 1998.

[34] M. O. Scully, *Quantum Optics*. Camebridge Universtiy Press, 1997.

[35] R. Loudon, *The Quantum Theory of Light*. Oxford Science Publications, 2000.

[36] Y. Zhao, *Resonance Fluorescence and Electron Spin in Semiconductor Quantum Dots*. PhD thesis, Natural Sciences and Mathematics of the Ruperto Carola-University of Heidelberg.

[37] W. Demtröder, *Laser Spectroscopy: Basic Concepts and Instrumentation*. Springer, 2003.

[38] C. Zeiss, "Die konfokale Laser Scanning Mikrosopie." `http://www.cai.hhu.de/fileadmin/redaktion/Fakultaeten/Mathematisch-Naturwissenschaftliche_Fakultaet/CAI/Literatur/Die_konfokale_Laser_Scanning_Mikroskopie.pdf`. [Online; accessed Juli-2013].

[39] R. H. Webb, "Confocal optical microscopy," *IOPSCIENCE*, vol. 59, p. 427, 1996.

[40] L. Novotny, "Nano Optics." `http://www.photonics.ethz.ch/en/courses/nanooptics.html`, 2006. [Online; accessed Juli-2013].

[41] Newport, "Light Collection and Systems Throughput." `http://www.newport.com/Tutorial-Light-Collection-and-Systems-Throughput/381845/1033/content.aspx`. [Online; accessed September-2013].

[42] rp photonics, "Single-mode Fibers." `http://www.rp-photonics.com/single_mode_fibers.html`. [Online; accessed August-2013].

[43] rp photonics, "External-cavity Diode Lasers." `http://www.rp-photonics.com/external_cavity_diode_lasers.html`. [Online; accessed August-2013].

[44] H. Ströker, "Stabilisierung der Emissionsfrequenz und Reduzierung der Linienbreite von Halbleiterlasern durch Rückreflexion von einem Stufengitter in Littrow-Anordnung," Master's thesis, Faculty of Applied Physics University Muenster.

[45] H. Wenz, "Aufbauf eines Diodenlasers mit externem Resonator zur Amplituden-/Phasenmodulations-Spektroskopie," Master's thesis, Faculty of Physics University Kaiserslauten.

[46] SSRL, "Biological X-Ray Absorption Spectroscopy." http://www-ssrl.slac.stanford.edu/smbxys/intrumentaion/cryoman.html. [Online; accessed Juli-2013].

[47] E. L. C. Palmer, "DIFFRACTION GRATING HANDBOOK." http://gratings.newport.com/library/handbook/toc.asp. [Online; accessed August-2013].

[48] Peter Y. Yu and Manuel Cardona, *Fundamentals of Semiconductors*. Springer.

[49] H. Föll, "Grundlagen der Materialwissenschaft für Elektro- und Informationstechniker." http://www.tf.uni-kiel.de/matwis/amat/mw_for_et/index.html. [Online; accessed August-2013].

[50] S. Seidl et al., "Absorption and photoluminescence spectroscopy on a single self-assembled charge-tunable quantum dot," *Physical Review B*, vol. 72, no. 195339, 2005.

[51] R. Warburton et al., "Giant permanent dipole moments of excitons in semiconductor nanostructures," *Phyiscal Review B*, vol. 65, no. 113303, 2002.

[52] M. Sciesiek et al., "Toward Better Light-Confinement in Micropillar Cavities," *ACTA PHYSICA POLONICA A*, vol. 120, p. 877, 2011.

[53] P. Eastham, "Nanophotonics I: quantum theory of microcavities." http://www.tcd.ie/Physics/people/Paul.Eastham/nanophotonics.pdf. [Online; accessed August-2013].

[54] B. Gayral and J. Gérard, "Photoluminescence experiment on quantum dots embedded in a large Purcell-factor microcavity," *Physical Review B*, vol. 78, no. 235306, 2008.

[55] G. Ctistis et al., "Optical characterization and selective addressing of the resonant modes of a micropillar cavity with a white light beam," *Physical Review B*, vol. 82, no. 195330, 2010.

[56] S. Reitzenstein, "cQED in Quantum Dot Micropillar Cavities - Fundamental Research and Applications." http://www.treasure-project.eu/wp-content/uploads/2011/09/PhotoNorth.pdf. [Online; accessed August-2013].

[57] C. Böckler et al., "Electrically driven high-Q quantum dot-micropillar cavities," *Optics Express*, vol. 92, no. 091107, 2008.

[58] M. Kroner et al., "Temperature dependent high resolutin resonant spectroscopy on a charged quantum dot," *Physica Status Solidi B*, vol. 246, p. 795, 2009.

[59] G. Ornter et al., "Temperature dependence of the excitonic band gap in InxGa1-xAs/GaAs self-assembled quantum dots," *Physical Review B*, vol. 72, no. 085328, 2005.

[60] R. Warburton et al., "Optical emission from a charge-tunable quantum ring," *Nature*, vol. 405, p. 926, 2000.

[61] B. Urbaszek et al., "Fine Structure of Highly Charged Excitons in Semiconductor Quantum Dots," *Physical Review*, vol. 90, no. 247403, 2003.

[62] W. Barnes et al., "Solid-state single photon sources: light collection strategies," *The European Physical Journal D*, vol. 18, p. 197, 2002.

[63] W. Gao et al., "Observation of entanglement between a quantum dot spin and a single photon," *Nature*, vol. 491, p. 426, 2012.

[64] M. Munsch, "Continuous-wave versus time-resolve measurements on Purcell-facotrs for quantum dots in semiconductor microcavities," *Physical Review B*, vol. 80, no. 115312, 2008.

[65] C. Mathiesen et al., "Subnatural Linewidth Single Photons from a Quantum Dot," *Physical Review Letters*, vol. 108, no. 093602, 2011.

[66] A. Muller et al., "Resonance Fluorescence from a Coherently Driven Semiconductor Quantum Dot in a Cavity," *Physical Review Letters*, vol. 99, no. 187402, 2013.

[67] O. Solgaard, *Photonic Microsystems: Micro and Nanotechnology Applied to Optical Devices and Systems*. Springer.